Heliyon 9 (2023) e20384

Contents lists available at ScienceDirect

Heliyon

journal homepage: www.cell.com/heliyon

RIT1 regulation of CNS lipids RIT1 deficiency Alters cerebral lipid metabolism and reduces white matter tract oligodendrocytes and conduction velocities☆

Lei Wu [a,1], Fang Wang [a,1], Carole L. Moncman [a], Mritunjay Pandey [a], Harrison A. Clarke [b], Hilaree N. Frazier [c], Lyndsay E.A. Young [a,d], Matthew S. Gentry [a,d,i,j], Weikang Cai [e], Olivier Thibault [c], Ramon C. Sun [b,d,f,i,j], Douglas A. Andres [a,d,g,h,*]

[a] Department of Molecular and Cellular Biochemistry, College of Medicine, University of Kentucky, KY 40536, USA
[b] Department of Neuroscience, College of Medicine, University of Kentucky, KY 40536, USA
[c] Department of Pharmacological and Nutritional Sciences, College of Medicine, University of Kentucky, KY 40536, USA
[d] Markey Cancer Center, Lexington, KY 40536, USA
[e] Department of Biomedical Sciences, New York Institute of Technology College of Osteopathic Medicine, NY 11568, USA
[f] Sanders-Brown Center on Aging, University of Kentucky, Lexington, KY 40536, USA
[g] Spinal Cord and Brain Injury Research Center, College of Medicine, University of Kentucky, KY 40536, USA
[h] Gill Heart and Vascular Institute, College of Medicine, University of Kentucky, Lexington, KY 40536, USA
[i] Department of Biochemistry and Molecular Biology, University of Florida, College of Medicine, Gainesville, FL 32611, USA
[j] Center for Advanced Spatial Biomolecule Research, University of Florida, College of Medicine, Gainesville, FL 32611, USA

ARTICLE INFO

Keywords:
Rit GTPase
Myelin
Oligodendrocyte progenitor cell
Lipidomics
Myelination
Endothelin-1
MALDI-MSI
Ras

ABSTRACT

Oligodendrocytes (OLs) generate lipid-rich myelin membranes that wrap axons to enable efficient transmission of electrical impulses. Using a *RIT1* knockout mouse model and *in situ* high-resolution matrix-assisted laser desorption/ionization mass spectrometry imaging (MALDI-MSI) coupled with MS-based lipidomic analysis to determine the contribution of RIT1 to lipid homeostasis. Here, we report that RIT1 loss is associated with altered lipid levels in the central nervous system (CNS), including myelin-associated lipids within the corpus callosum (CC). Perturbed lipid metabolism was correlated with reduced numbers of OLs, but increased numbers of $GFAP^{+}$ glia, in the CC, but not in grey matter. This was accompanied by reduced myelin protein expression and axonal conduction deficits. Behavioral analyses revealed significant changes in voluntary locomotor activity and anxiety-like behavior in $RIT1^{KO}$ mice. Together, these data reveal an unexpected role for RIT1 in the regulation of cerebral lipid metabolism, which coincide with altered white matter tract oligodendrocyte levels, reduced axonal conduction velocity, and behavioral abnormalities in the CNS.

☆ The authors have declared that no conflict of interest exists.

* Corresponding author. Department of Molecular and Cellular Biochemistry BBSRB B149, University of Kentucky, KY 40536, USA.
E-mail address: dandres@uky.edu (D.A. Andres).

[1] Equal contribution.

https://doi.org/10.1016/j.heliyon.2023.e20384
Received 13 December 2022; Received in revised form 21 July 2023; Accepted 20 September 2023
Available online 23 September 2023

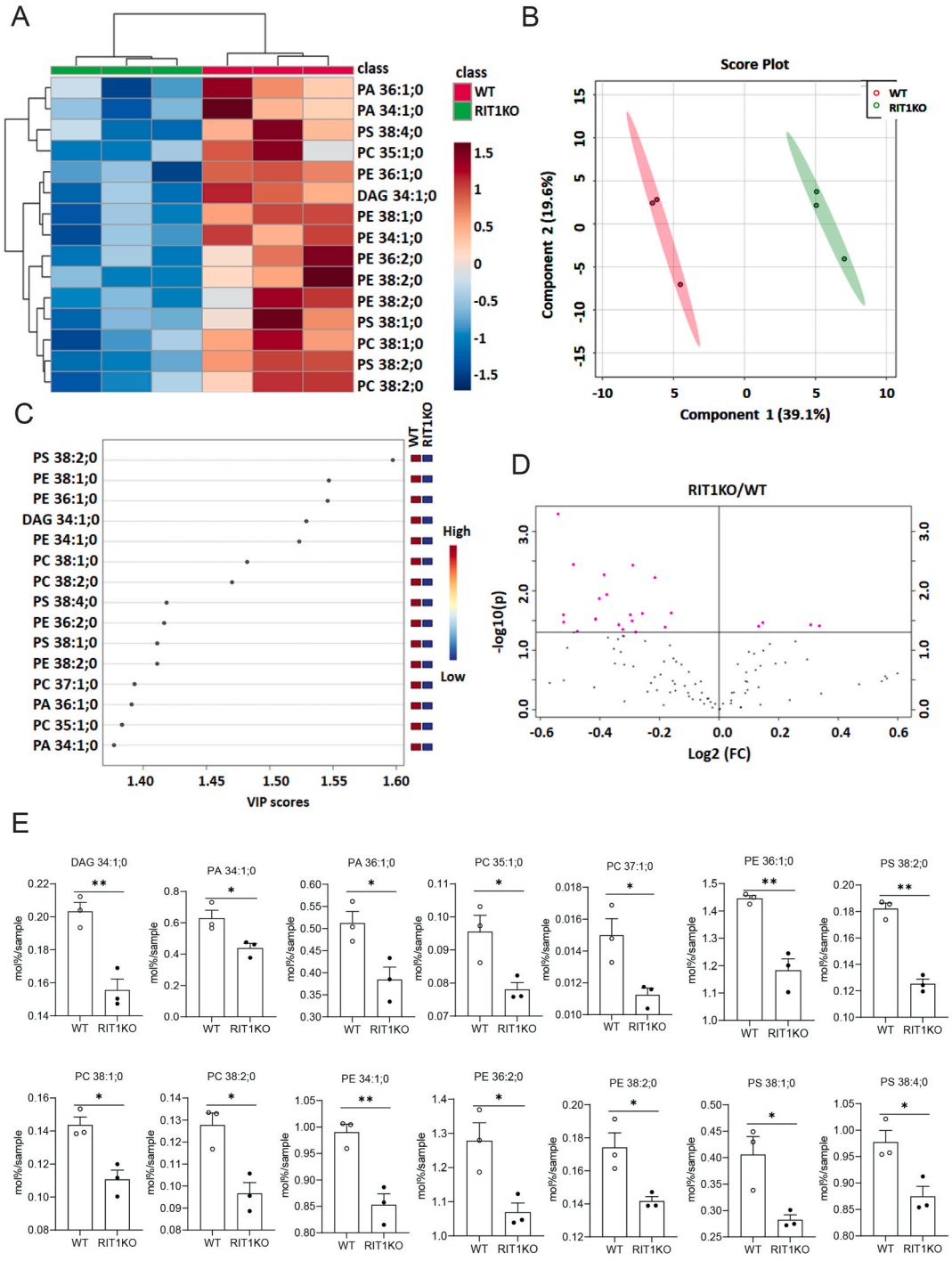

Fig. 1. Shotgun lipidomics analysis of WT and *RIT1*^{KO} mouse brains. (A) Two-dimensional clustering heatmap analysis of phospholipids between adult WT and *RIT1*^{KO} brains (n = 3 per genotype). Top 15 most changed (by one-way ANOVA with *post hoc* Tukey-Kramer multiple comparisons) phospholipids are shown. (B) Partial least squares discriminant analysis (PLS-DA) of lipids between WT (red) and *RIT1*^{KO} (green) brain samples; 95% confidence interval for each group is shown as shaded areas using the same color as representative groups. (C) Variable importance in projection (VIP) analysis showing the contribution of top 15 most changed phospholipids to PLA-DA clustering in (B). (D) Volcano plot showing fold change between *RIT1*^{KO}/WT. Phospholipids with either 1.5-fold increase or decrease with -log10(p value) > 1.2 are highlighted in pink. (E) Summary graphs to showing significantly reduced phospholipids between WT and RIT1^{KO} mouse brains. Data is presented as the mean ± SEM. *$p < 0.05$, **$p < 0.01$ by two-tailed unpaired t-test.

1. Introduction

Oligodendrocytes (OLs) originate from oligodendrocyte progenitor cells (OPCs) within the subventricular zone, which proliferate and migrate throughout the CNS [1,2]. In response to diverse cellular signals, OPCs differentiate to mature OLs that function to myelinate adjacent axons, a process that wraps axons in a multi-layer membrane structure [3]. Myelination provides the insulation that enables efficient action potential propagation while also providing metabolic support [4,5]. Alterations in myelin structure have been found to impact axonal conduction, and loss of myelin may induce pathologies such as multiple sclerosis [6].

OPC migration and differentiation is under the control of both intrinsic and extrinsic factors [7], with members of the Ras

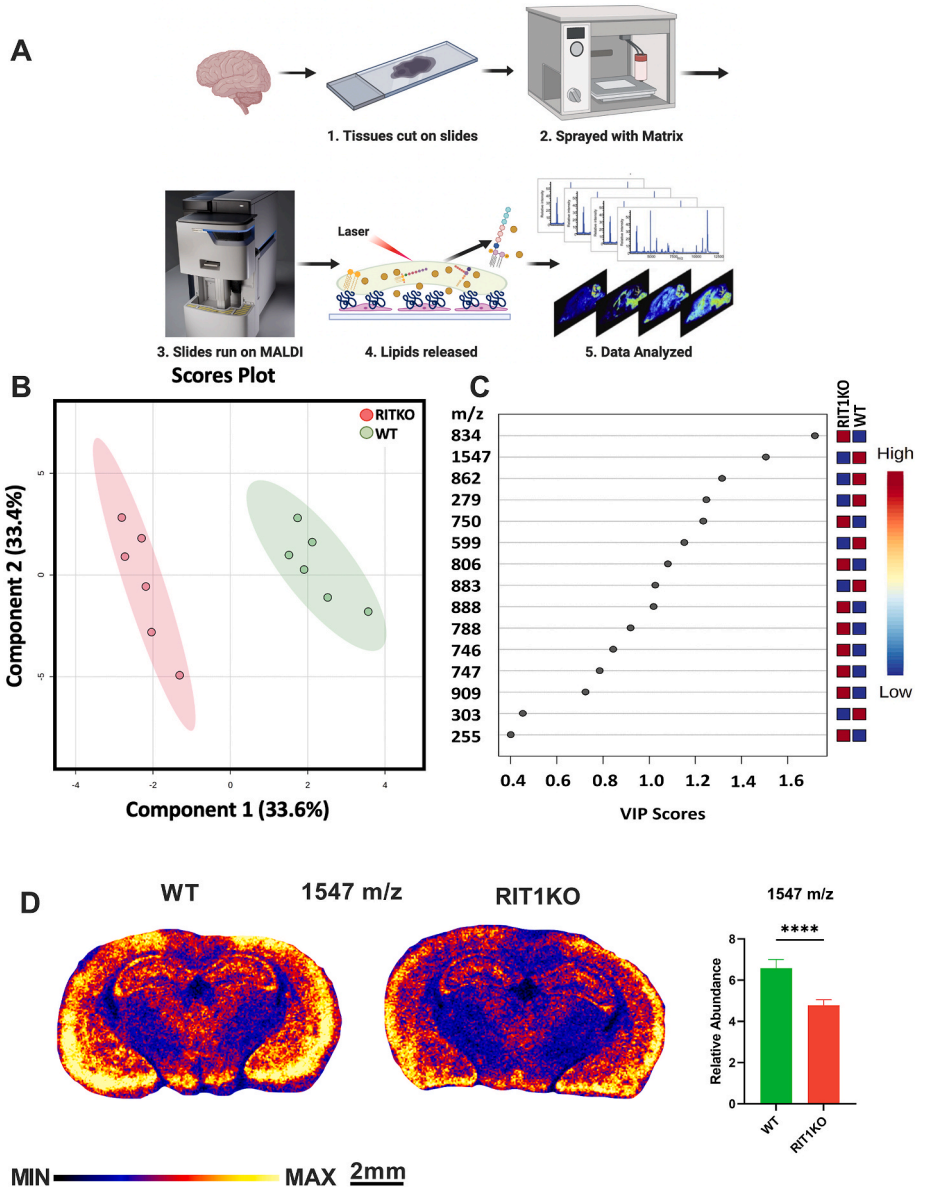

Fig. 2. MALDI-MSI analysis identifies altered lipids levels in *RIT1*^{KO} mice. (A) Graphical schematic of MALDI-MSI workflow for the spatial profiling of lipids in brain sections. Adult mouse brains (3–4 months) were frozen, sectioned into 10 μm slices, mounted onto charged microscope slides, dry sprayed with CHCA matrix and directly analyzed by MALDI-MSI. (B) Partial least squares discriminant analysis (PLS-DA) of lipids between WT (green) and *RIT1*^{KO} (red) mouse hippocampi. 95% confidence interval for each group are shown as shaded areas using the same color as respective groups. Three technical replicates extracted from regions of interest (ROIs) in the hippocampus of WT and *RIT1*^{KO} mice were collected and averaged. (C) Variable importance in projection (VIP) analysis displaying the top 15 lipids contributing to the PLS-DA clustering. (D) Left: Spatial distribution of a glycosphingolipid (*m/z* 1547) from WT and *RIT1*^{KO} mouse brains. Scale bar is represented below the images. The image displays a heatmap gradient of intensity with black (least abundant) to yellow (most abundant). Right: The relative abundance of *m/z* 1547. Data shown represents the mean ± the standard error of the mean (SEM) of n = 3 ROIs per mouse. ****p < 0.0001; unpaired, two-tailed *t*-test.

superfamily of small guanosine triphosphatases (GTPase) [8–12] identified as one critical component of the complex regulatory network involved in controlling OL maturation and myelination [2]. A key feature of myelin is high lipid content [2,13,14], and axonal myelination requires high levels of fatty acid the generation of large quantities of lipid, with OLs involved in synthesizing nearly half of total brain lipid [14]. While there are no myelin-specific lipids, the composition of the myelin sheath is distinctive, with high amounts of cholesterol and enriched in glycolipids, compared to most biological membranes, with the most abundant lipids being cholesterol, galactosylceramide, and plasmogen [15]. This enrichment in specific lipid classes is required for the long-term maintenance of myelin [14]. As myelin lipids are continuously remodeled, their biosynthesis, storage and trafficking play essential roles in myelin assembly and to sustain myelin sheaths through life. The high lipid/protein ratio in myelin contributes to the organization of the sheath, which together with the actions of a collection of myelin-specific proteins [16] affect myelin function.

The Ras family of small GTPases is a group of evolutionarily conserved enzymes that serve as molecular switches that undergo guanine-nucleotide-dependent conformational change [17]. Functioning with their affiliated regulatory [18] and effector protein networks, Ras-related GTPases serve to couple diverse cellular stimuli to the regulation of select signal transduction pathways, making critical contributions to cellular physiology [19]. Ras GTPases are crucial regulators of the RAF/MEK/ERK signaling cascade with gain-of-function mutations observed in a host of human cancers [19] and a group of developmental disorders, termed RASopathies [20]. The Ras-related G-protein, RIT1, is widely expressed, including throughout the CNS and within the developing brain [21,22]. At the genetic level, somatic and germline mutations in *RIT1* have been discovered [23,24], and recent studies have demonstrated that *RIT1* mutations contribute to the developmental disorder Noonan syndrome [23,25], a RASopathy, and to cancers including lung adenocarcinoma [24,26] and myeloid malignancies [23,27]. Despite its widespread expression, the physiological role for *RIT1* remains incompletely characterized [21,22]. Within the CNS, we have identified roles for RIT1 in the regulation of axonal and dendritic growth [28,29], neuronal stress-dependent MAPK activity [30–33], pro-survival signaling [34–36], and IGF-1 and exercise-dependent hippocampal neurogenesis via activation of a SOX2 transcriptional cascade [37,38].

Here, we report an unexpected role for RIT1 in the regulation of cerebral lipid levels and white matter tract neuroglia. $RIT1^{KO}$ mice exhibit select increases in $GFAP^{+}$-astrocytes and decreases in mature OLs in the corpus callosum (CC) without a significant difference in cell density within the cortex when compared with controls. $RIT1^{KO}$ mice also display reduced voluntary locomotor activity accompanied by altered myelin-associated protein expression and diminished conduction velocities in axonal tracts of the CC. Taken together, our data reveal that RIT1 contributes to the regulation of brain lipid metabolism, and show that RIT1 loss coincides with altered glial subtype densities in white matter tracts, suggesting that RIT1 may play a role in brain myelinogenesis.

2. Results

2.1. Absence of RIT1 alters cerebral lipid composition

Within the subventricular zone (SVZ) there are transcriptional differences in lipid metabolic genes between quiescent and activated neural stem cells (NSCs) [39], and defects in lipid metabolism have been shown to disrupt NSC proliferation and neurogenesis [40]. As *RIT1* signaling contributes to the regulation of exercise- and IGF-1-dependent hippocampal neurogenesis [34,37,40,41] we were interested in exploring whether RIT1 signaling might regulate lipid metabolism. To determine whether RIT1 contributes to the regulation of CNS lipid levels, brain samples from wild-type and $RIT1^{KO}$ mice were analyzed using a shotgun MS-based lipidomics approach (Lipotype GmbH) [42], which has the capacity to identify a great number of lipid classes and specific lipid species. To our surprise, multivariate analysis identified opposing clustering between the cerebral lipid profiles of wild-type and $RIT1^{KO}$ mice from both unsupervised two-dimensional heatmap (Fig. 1A) and partial least squared discrimination analyses (PLS-DA) (Fig. 1B) analyses. Variable importance in projection (VIP) analysis and volcano plots confirmed a consistent decrease in lipids within *RIT1* knockout mice

Table 1
Summary of composition, *m/z* values, and class for brain. lipids detected by MALDI.

m/z	Lipid Class	Chain Lengths	Accurate Mass	Mass Accuracy Delta
255.2444	FA	(16:0)	256.2	0.9556
279.9736	FA	(18:2)	280.2	0.2264
281.2548	FA	(18:1)	282.5	1.2452
303.2345	FA	(20:4)	304.5	1.2655
599.2463	LPI	(18:0)	600.3	1.0537
746.3925	PEp	38:6(16:0p/22:6)	746.5	0.1075
747.3788	PG	34:1(16:0/18:1)	747.5	0.1212
750.4169	PEp	38:4(16:0p/22:4)	750.5	0.0831
788.4103	PS	36:1(18:0/18:1)	788.5	0.0897
806.4074	Sulfatide	(d18:1/C18:0)	806.6	0.1926
834.3902	Sulfatide	(d18:1/C20:0)	834.5	0.1098
857.3625	PI	36:4(16:0/20:4)	857.5	0.1375
862.4513	Sulfatide	(d18:1/C22:0)	862.6	0.1487
883.3719	PI	38:5(18:1/20:4)	883.5	0.1281
885.3875	PI	38:4(18:0/20:4)	885.5	0.1125
888.4593	Sulfatide	(d18:1/C24:1)	888.6	0.1407
909.4704	PI	40:6(18:0/22:6)	909.5	0.0296
1547.4953	GSL	18:1/18:0	1546.8	0.6953

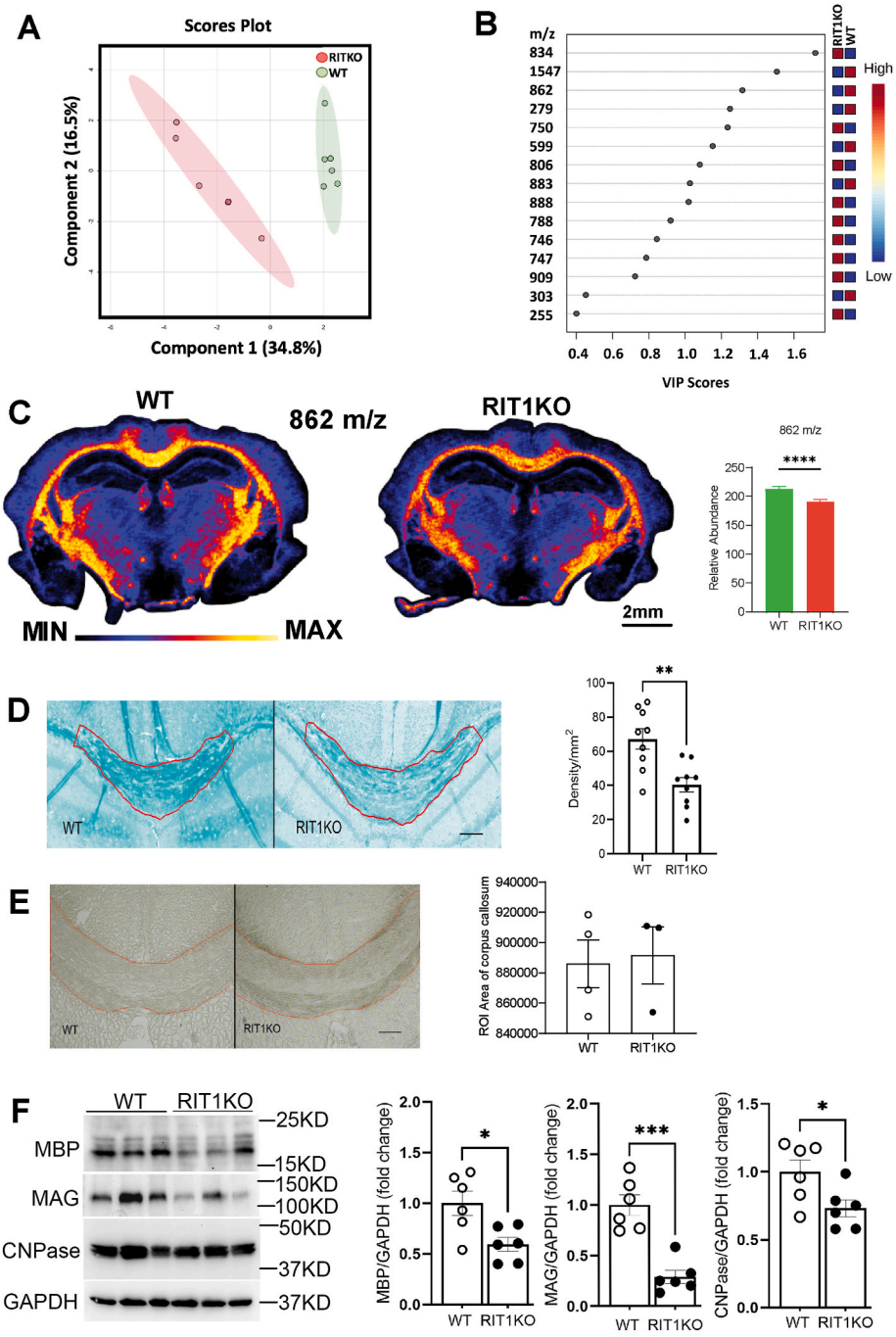

Fig. 3. RIT1^{KO} does not affect overall corpus callosum thickness but reduces myelin protein levels. (A) Partial least squares discriminant analysis (PLS-DA) of lipid between WT (green) and *RIT1*^{KO} (red) mouse corpus callosum. 95% confidence interval for each group are shown as shaded areas using the same color as the respective groups. (B) Variable importance in projection (VIP) analysis showing 15 lipids contributing to the PLS-DA clustering. (C) Spatial distribution (*left*) of lipid *m/z* 862 from WT and *RIT1*^{KO} mouse brains. Scale bar is represented below the images. The image displays a heatmap gradient of intensity with black (least abundant) to yellow (most abundant). (*Right*) The relative abundance of *m/z* 862. Data shown represents the mean ± SEM of n = 3 per group. ****$p < 0.0001$; unpaired, two-tailed T test. (D) Representative images for Luxol Fast Blue (LFB) stained coronal sections of control (wild-type, WT) and *RIT1*^{KO} mouse brains. Quantification of LFB staining from the corpus callosum. Data shown represent mean ± SEM of n = 9 per group. **p < 0.001; unpaired two-tailed T test. (E) Representative bright field images and volume quantification of the corpus callosum from control (WT) and *RIT1*^{KO} adult mice (mean ± SEM; n = 3). Scale bars = 250 μm. (F) Immunoblotting and quantification of myelinating proteins MAG, MBP and CNPase in WT and *RIT1*^{KO} brain lysates. Data shown represents the mean ± SEM of n = 6 per group. *$p < 0.05$; unpaired, two-tailed T test.

(Fig. 1C and D). Furthermore, targeted analysis of the relative abundance of multiple lipids highlighted by VIP analysis detected profound decreases in many cerebral lipids in *RIT1*^{KO} mice (Fig. 1E). Collectively, MS lipidomics data suggests that *RIT1* loss results in a fundamental shift in cerebral lipid expression.

To confirm and extend these results, *in-situ* spatial analysis of lipids using matrix-assisted laser desorption ionization-mass spectrometry imaging (MALDI-MSI) was used to examine CNS lipids at 50 μm resolution. Using this method to understand changes in lipids within specific anatomical brain regions (Fig. 2A), we were able to detect 18 general lipid species (Table 1) in the hippocampus (Fig. 2B) of wild-type (WT) and *RIT1* knockout (*RIT1*^{KO}) mice [35]. We extracted three regions of interest that correspond to ~70 pixels or 70 unique data points from each mouse hippocampi (Fig. S1) andperformed multivariate analyses to identify major lipid changes between WT and *RIT1*^{KO} mice. Partial least squared discrimination analyses (PLS-DA) identified distinct separation between the WT and *RIT1*^{KO} data (Fig. 2B). Lipid species that are most altered are highlighted by VIP analysis and ranked by VIP score (Fig. 2C). Targeted analysis of the relative abundance of multiple lipids highlighted by VIP analysis display profound differences in the hippocampus of WT and *RIT1*^{KO} mice (Fig. 2D). Next, we performed similar analyses in the cortex of WT and *RIT1*^{KO} mice (Fig. S2). Like the hippocampus, heatmap, PLS-DA, and VIP analyses demonstrated major changes in lipid expression between the cortices of WT mice and *RIT1*^{KO} mice (Fig. S2A-C). These data suggest that *RIT1* deficiency results in a fundamental shift in both the spatial distribution and expression of various CNS lipids.

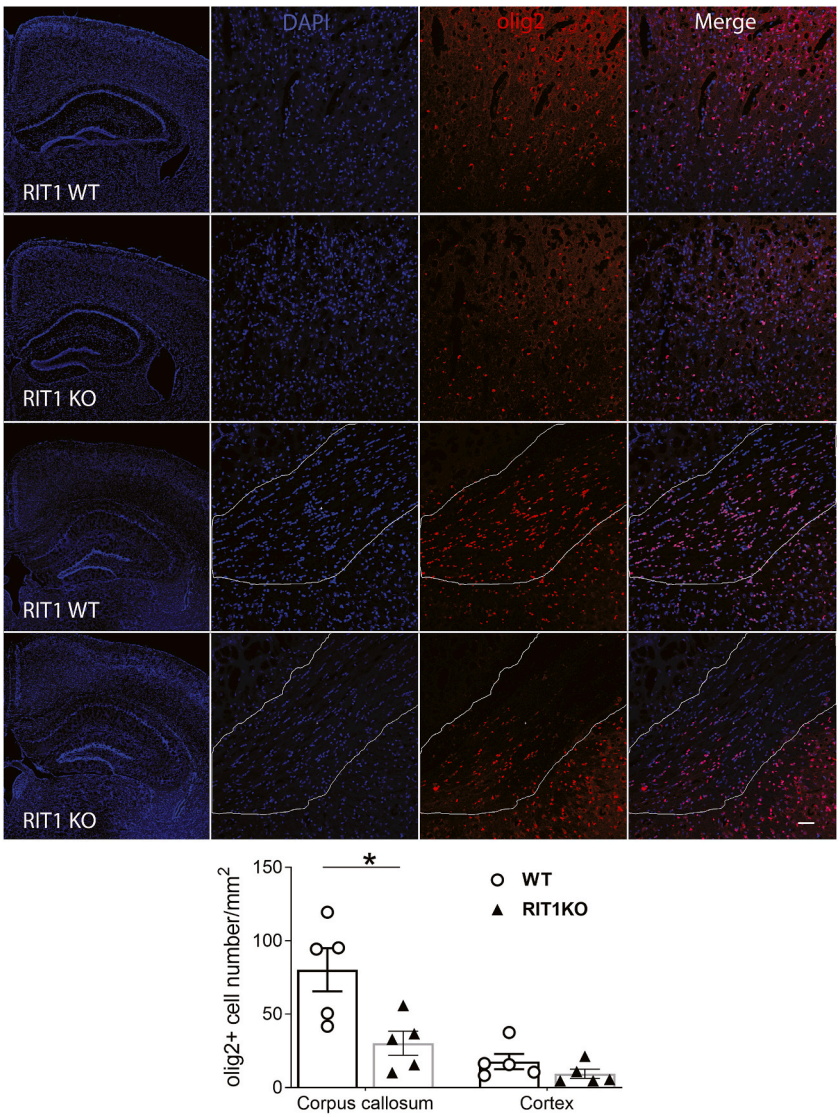

Fig. 4. RIT1 deficiency reduces oligodendrocyte lineage cell density in the corpus callosum. Dual-labeled representative images for the pan-oligodendrocyte marker, Olig2, and DAPI in the cortices and corpus callosum of WT and *RIT1*^{KO} mice. Note the decreased density of Olig2^{+} cells in the corpus callosum, but not the cortex, of *RIT1*^{KO} mice, relative to controls (white boxes, mean ± SEM; n = 3, *$p < 0.05$, unpaired, two-tailed *t*-test). All scale bars = 100 μm.

2.2. Loss of RIT1 causes a reduction in myelin-associated proteins

Myelin contains a high concentration of lipids, and the formation of the myelin sheath requires high levels of lipid synthesis [43]. Targeted analysis of the relative abundance of multiple lipids by MALDI-MSI analysis indicated that levels of glycosphingolipids and sulfatides, major lipid components of myelin [44], were reduced within the corpus callosum of *RIT1*^{KO} mice (Fig. 3A–C), suggesting that RIT1 loss might affect myelination. Levels of myelination within the CNS was examined by Luxol Fast Blue (LFB) staining [45]. Representative images and quantitative analysis (Fig. 3D) of coronal brain sections showed a robust loss of myelin staining in *RIT1* null mice when compared to wild-type controls. Histological analysis failed to detect an alteration in the thickness of the corpus callosum in *RIT1* null mice compared to controls (Fig. 3E). However, Western blot analysis from total brain homogenates found that levels of

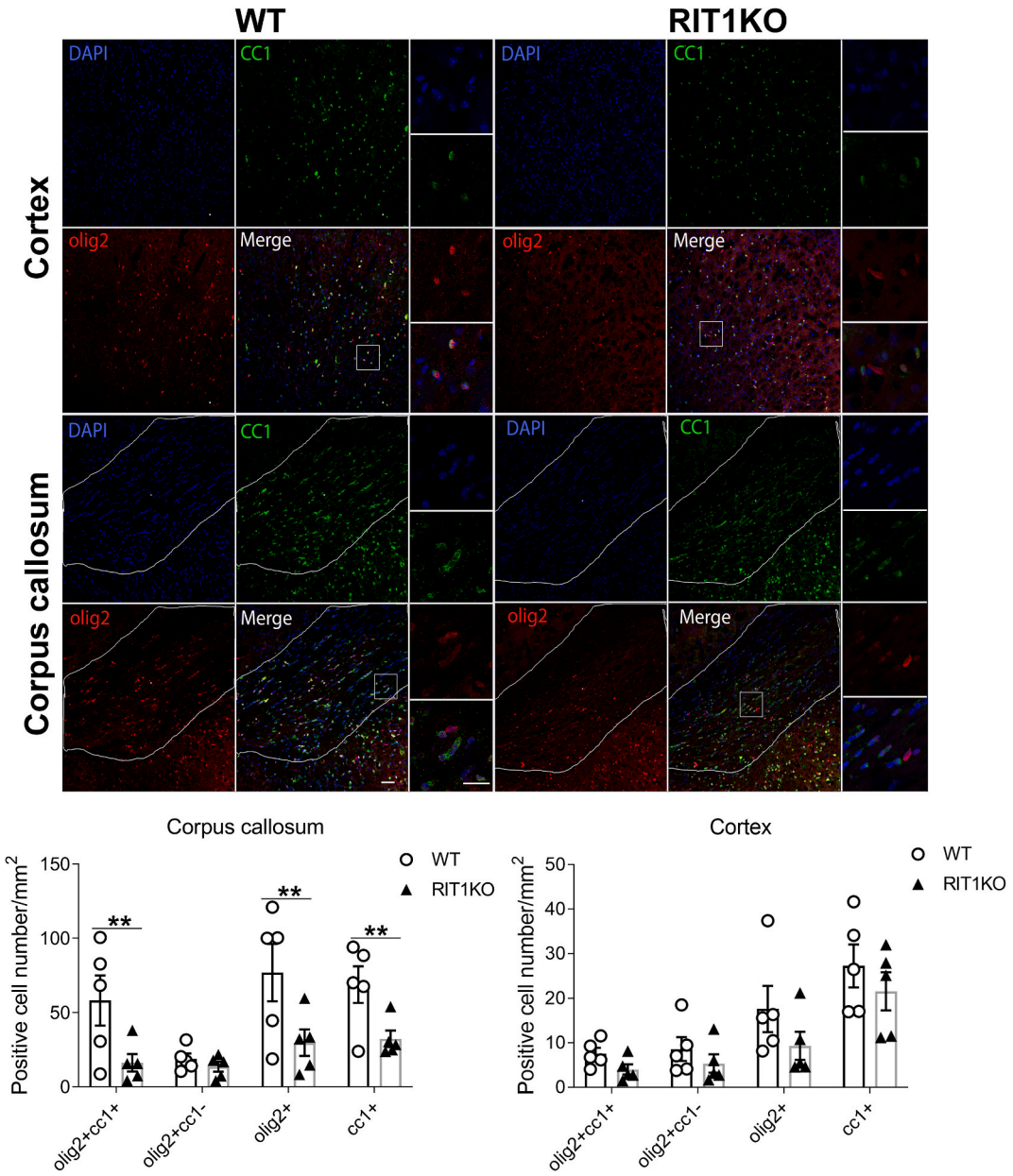

Fig. 5. RIT1 deletion results in a significant reduction in myelinating oligodendrocytes in the corpus callosum. Triple-labeled representative images of control (WT; *left panels*) and mutant (*RIT1*^{KO}; *right panels*) for the pan-oligodendrocyte marker, Olig2, mature myelinating marker, CCI, and DAPI. Analysis of CC1^{+} cells revealed a significant reduction in the number of presumably mature, myelinating oligodendrocytes in the corpus callosum, but not the cortex, of *RIT1*^{KO} mice, relative to controls. Scale bars = 100 μm. High magnification (white box) scale bars = 10 μm. Assessment of Olig2^{+}/CC1^{+} oligodendrocyte lineage cells revealed a significant decrease in the density within the *RIT1*^{KO} corpus callosum relative to age-matched controls (mean ± SEM; n = 3, *$p < 0.05$, by two-tailed unpaired *t*-test).

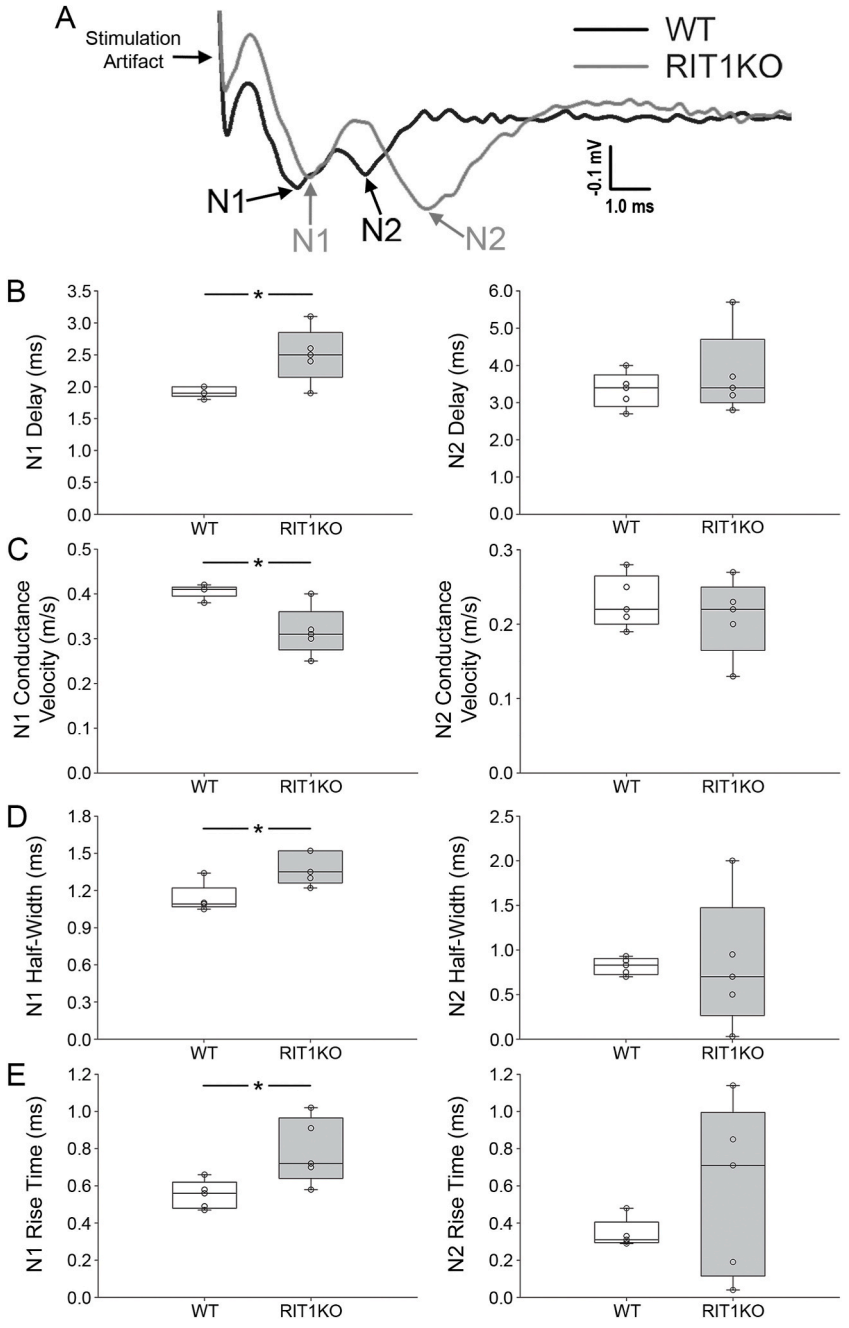

Fig. 6. RIT1 deletion causes slowed conduction velocity within the corpus callosum. (A) Representative fEPSPs recorded within the corpus callosum of coronal slices taken from a WT (black line) and $RIT1^{KO}$ (grey line) adult mouse (3–4 months). Stimulating electrodes were placed near the midline with recording electrodes positioned ~0.75 mm ipsilaterally. Responses were obtained using 0.33 Hz stimulation with an intensity set to 50% of the maximal response of the slice. Stimulation artifacts were truncated for display purposes to better visualize the fEPSPs. Labels indicate the locations of the N1 and N2 peaks for each representative trace. The fastest N1 component is comprised of myelinated axons and is followed by the slower N2 component, comprised of nonmyelinated axons. (B–E). Measures of Delay, Conductance Velocity, Half-Width, and Rise Time for N1 (*left*) and N2 (*right*) responses recorded in a total of 10 animals (n = 5 animals per group). Statistical analysis revealed a significant impact of genotype across all 4 measures of the N1 response, as indicated by $RIT1^{KO}$ mice having larger response delays (Student's t-test; $p = 0.018$), reduced conduction velocities ($p = 0.009$), larger peak half-widths ($p = 0.014$), and slower peak rise times ($p = 0.025$) compared to control (WT) animals. Analysis of N2 responses from these same animals showed no differences between groups across any of the measures tested here (Student's t-test; $p > 0.05$).

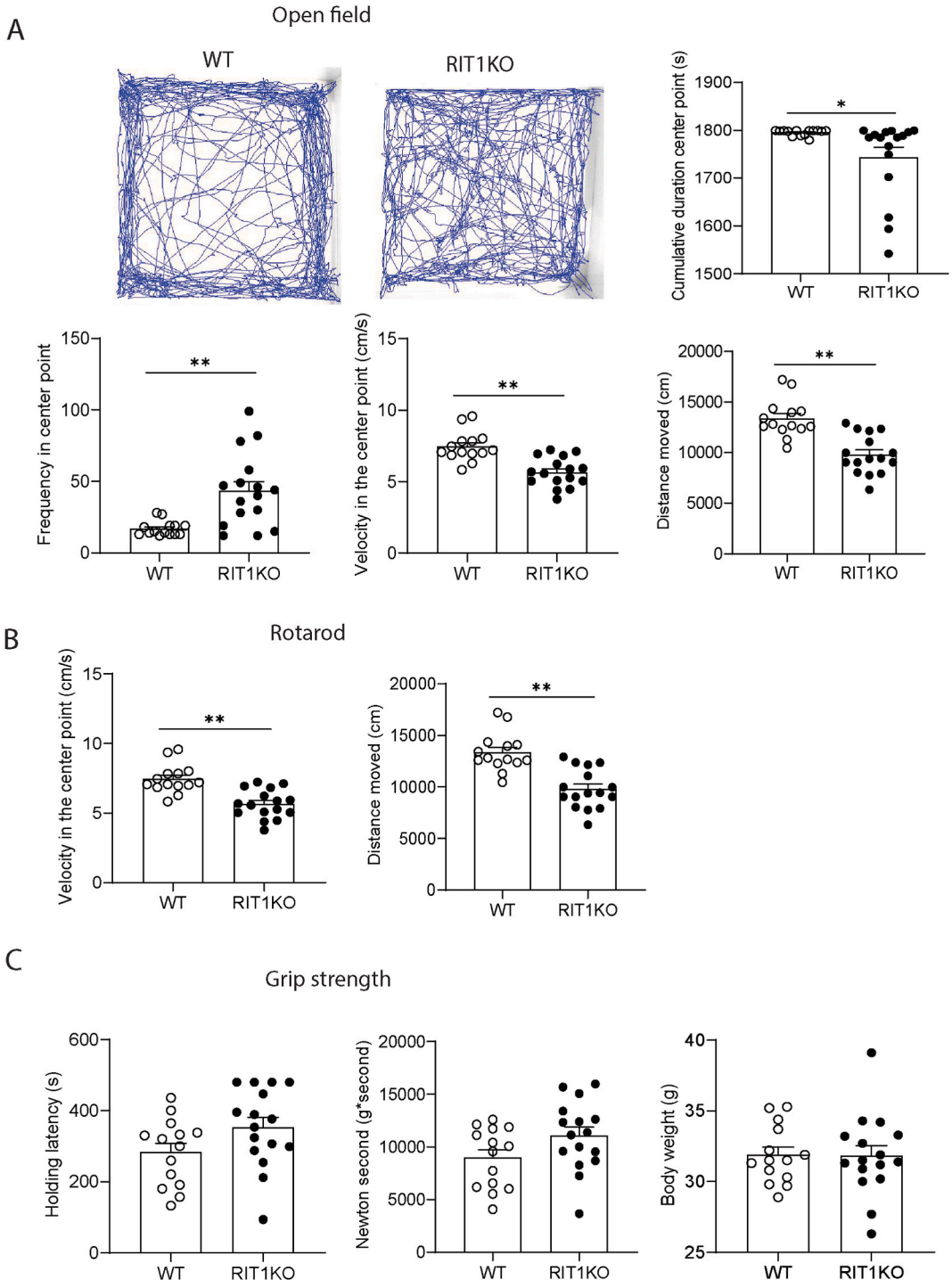

Fig. 7. *RIT1*^{KO} mice display locomotor deficits. Control (WT; n = 14) and *RIT1*^{KO} (n = 16) adult male mice (3–4 months) were tested on a battery of behavioral tasks including the open field, rotarod, and grip strength. (A) Representative track plots from a single mouse in each group. (B–D) In the open field test, *RIT1*^{KO} mice exhibited differences in (B) total distance traveled, (C) velocity, and (D) frequency in the center point from controls. (E) Accelerating rotarod testing revealed that *RIT1*^{KO} mice display impaired motor coordination, as measured by latency and total distance. (F) In the wire hang grip strength test, control and *RIT1*^{KO} mice display similar performance. Data shown represents the mean ± SEM of n = 14–16 per group. *$p < 0.05$, **$p < 0.01$. Unpaired, two-tailed T test.

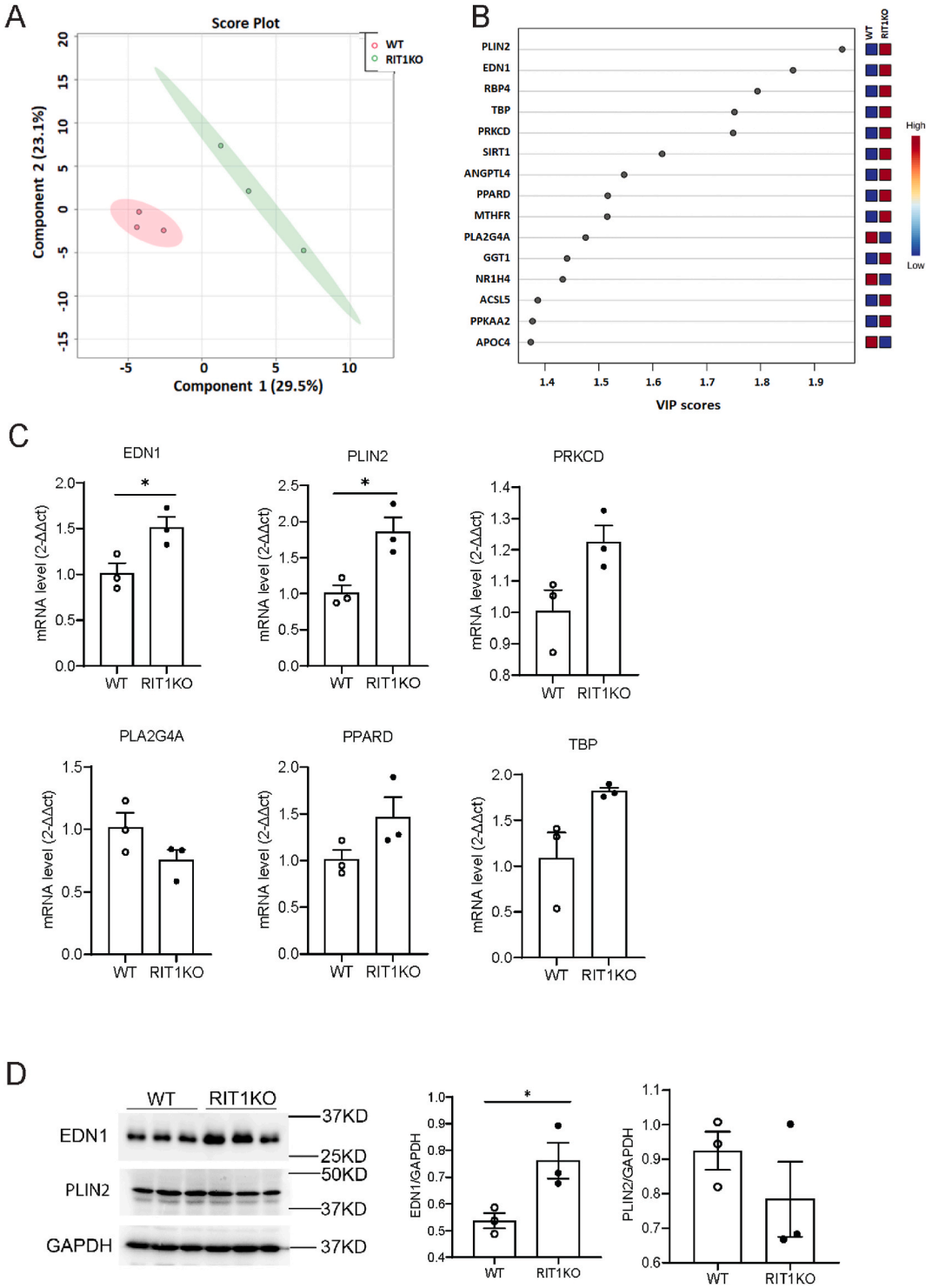

Fig. 8. Endothelin-1 increased in *RIT1*^{KO} brains. (A) Partial least squares discriminant analysis (PLS-DA) of lipid metabolism-focused gene expression between WT (red) and *RIT1*^{KO} (green) brains; 95% confidence interval for each group is shown as shaded areas using the same color as representative groups. (B) Variable importance in projection (VIP) analysis of the top 17 gene expression differences that contribute to PLS-DA clustering in (A). (C) Secondary qRT-PCR validation analysis of the gene expression differences between WT and *RIT1*^{KO} brains. (D) Western blot analysis and quantification of EDN1 and PLIN2 protein levels in WT and *RIT1*^{KO} brain lysates. Data shown represent the mean ± SEM of n = 3 per group. *$p < 0.05$; unpaired, two-tailed *t*-test.

myelin basic protein (MBP), myelin-associated glycoprotein (MAG), and expression of 2′, 3′-cyclic nucleotide 3′-phosphodiesterase (CNP), all membrane-associated proteins abundantly expressed in myelin-forming OLs, were significantly lower in *RIT1*^{KO} mice compared with wild-type mice (Fig. 3F and Supplemental Fig. S3). Taken together, these data suggest that *RIT1* loss affects myelination.

2.3. Oligodendrocyte population is reduced in the corpus callosum of *RIT1*^{KO} mice

As OLs are responsible for myelin production in the CNS, we next asked whether *RIT1* loss affected oligodendrogenesis. To determine whether RIT1 loss altered oligodendroglial cell numbers, we performed oligodendroglial-specific Olig2 immunohistochemical staining in coronal sections from wild-type and *RIT1*^{KO} mice (Fig. 4). Histological examination revealed a selective decrease in oligodendroglial cell density in the corpus callosum (WT 80.19 ± 32.91 vs RIT1^{KO} 30.14 ± 18.23, $p = 0.024$), of knockout mice, but not the cortex (WT 17.60 ± 11.60 vs RIT1^{KO} 9.31 ± 7.12, $p = 0.218$) (Fig. 4). To further assess the role of *RIT1* in OL differentiation *in vivo*, we distinguished between myelinating and immature lineage cells by co-labeling with the mature oligodendrocyte marker, CC1 [46]. As expected, the population of CC1^{+} OLs was reduced in the corpus callosum (WT 68.86 ± 27.56 vs *RIT1*^{KO} 32.37 ± 12.42, $p = 0.038$), but not the cortex of *RIT1*^{KO} mice (WT 27.25 ± 10.77 vs *RIT1*^{KO} 21.56 ± 9.22, $p = 0.404$). Furthermore, double immunohistochemical staining with anti-Olig2 and anti-CC1 antibodies displayed a significant reduction in the proportion of mature OLs (Olig2^{+}/CC1^{+}) within the overall oligodendroglial cell number in the corpus callosum (WT 62.21 ± 31.82 vs RIT1^{KO} 16.16 ± 12.22, $p = 0.028$), but not in the cortex of *RIT1*^{KO} mice when compared with wild-type controls (WT 7.54 ± 2.92 vs RIT1^{KO} 3.99 ± 2.57, $p = 0.076$) (Fig. 5). These data support a role for *RIT1* in the maintenance of oligodendroglial populations in the corpus callosum.

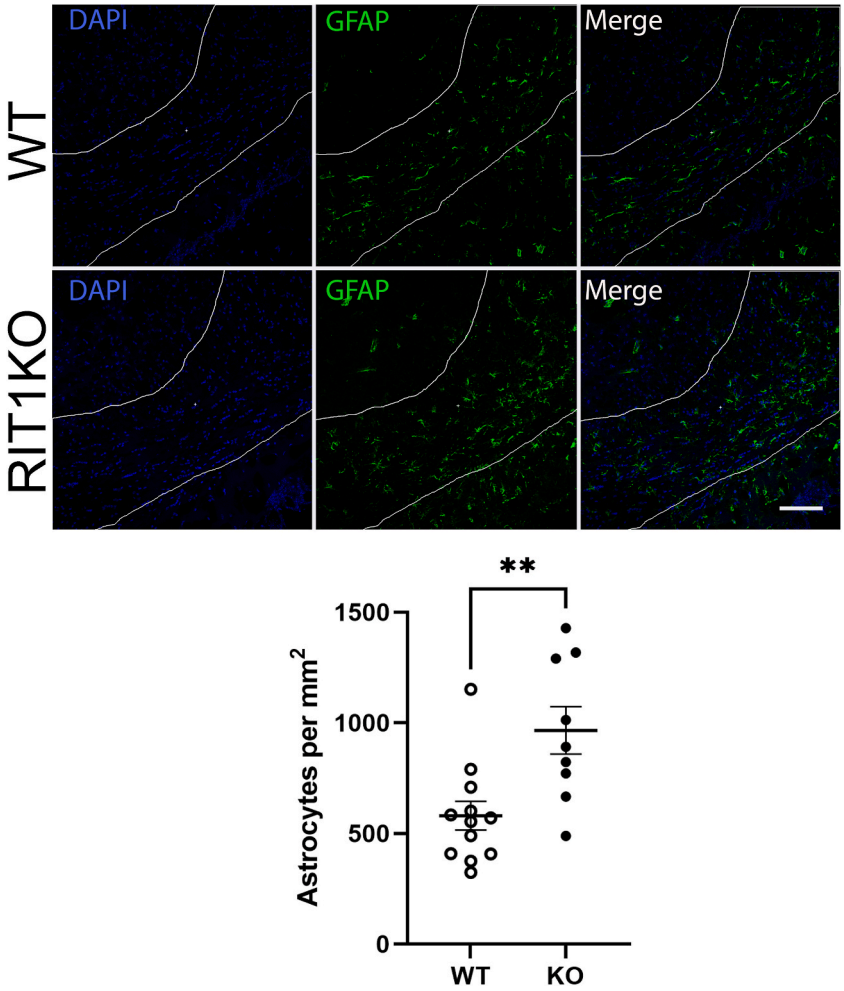

Fig. 9. RIT1 deficiency results in increased GFAP $^{+}$ astrocytes in the corpus callosum. Brain sections from control (WT) and *RIT1*^{KO} were stained for GFAP and DAPI. Representative images of each genotype are shown with the corpus callosum outlined. Quantification of the GFAP signal show a significantly increased density of GFAP $^{+}$ astrocytes in the *RIT1*^{KO} corpus callosum (966 ± 107, n = 4, vs. 580 ± 65, n = 4 $^{**}p < 0.01$). Scale bar = 10 μm.

2.4. *RIT1* deficiency results in conduction deficits in the corpus callosum

To assess the effect of *RIT1* loss on axonal function in the corpus callosum, the compound action potential (CAP) velocity and amplitude were evaluated in *ex vivo* slices from wild-type and $RIT1^{KO}$ mice. The CAP waveform has two components: N1 is predominantly comprised of fast-conducting myelinated axons, while N2 includes slower-conducting, generally non-myelinated axons (Fig. 6A). Measures of I/O slopes were similar across groups (data not shown; $p > 0.05$). Representative waveforms indicated that N1 responses recorded in the CC appeared to be slower in $RIT1^{KO}$ mice compared to WT, as highlighted by larger response delays and reduced conduction velocities (Fig. 6B and C; Student's t-test; $p = 0.018$ and 0.009, respectively). Additionally, knockout of *RIT1* was associated with significant increases in N1 half-widths and rise times (Fig. 6D and E; Student's t-test; $p = 0.014$ and 0.025, respectively), likely due to the slower responses observed in these animals. No significant differences were detected on measures of N1 amplitude peak or slope (data not shown). As expected, recordings of N2 did not appear to differ between genotypes across any of the measures tested here ($p > 0.05$), likely due to the contribution of slower, non-myelinated axons that would be unaffected by the loss of mature oligodendrocytes observed in *RIT1* knockout white matter tracts. The combination of both N1 and N2 amplitudes was not significantly different between genotypes, suggesting that overall axon numbers were not altered by *RIT1* deletion. Together, these data demonstrate slowed conduction velocity, but no reduction in axon number, in the corpus callosum of $RIT1^{KO}$ mice. These data further support the notion that RIT1 deficiency may affect myelination.

2.5. $RIT1^{KO}$ mice display a locomotive deficit

Neural circuits that underlie sensorimotor, cognitive, and emotional function depend on myelination to coordinate action potential conduction [47], with deficits in myelination often resulting in motor deficits [48,49]. To evaluate whether the changes in nerve conduction velocity in $RIT1^{KO}$ mice had functional consequences, we assessed anxiety-like and locomotor behavior (Fig. 7). In an open field assay [50], $RIT1^{KO}$ mice displayed a significant decrease in total distance traveled and velocity, but an increase in the time spent in the center quadrant of the field (Fig. 7A–D). These data were consistent with the rotarod test, a separate measure of motor performance, which found a significant reduction in both distances traveled and latency between $RIT1^{KO}$ and wild-type mice (Fig. 7E). Grip strength was not significantly different between knockout and control mice, suggesting that the reduction in rotarod performance in $RIT1^{KO}$ mice was not the result of a deficit in muscle strength (Fig. 7F). Cumulatively, $RIT1^{ko}$ mice demonstrate moderately increased anxiety-like behavior and a deficit in voluntary locomotor function.

2.6. Upregulation of endothelin 1 and increased $GFAP^+$ astrocytes in $RIT1^{KO}$ mice

As *RIT1* is known to control the activity of multiple transcription factors [32,33,37,38], we hypothesized that the lipid alterations observed in $RIT1^{KO}$ mice were the result of altered gene expression. To test this hypothesis, we performed a pathway-focused PCR array analysis to identify differences in the expression of 91 enzymes implicated in lipid metabolism. Multivariate analysis demonstrated distinct gene expression patterns between WT and $RIT1^{KO}$ mice by PLS-DA (Fig. 8A). The top 15 most changed genes revealed by VIP analysis are listed in Fig. 8B. Secondary evaluation by quantitative RT-PCR (Fig. 8C) found that the expression of endothelin 1 (*EDN1*) and perilipin 2 (*PLIN2*) to be significantly upregulated following genetic ablation of *RIT1*. Western blot analysis of total brain lysates failed to confirm a change in perilipin2 protein expression, but endothelin-1 levels were significantly elevated in $RIT1^{KO}$ mice when compared to WT mice (Fig. 8D and Supplemental Fig. S4). Astrocytes are the main cell type responsible for ET-1 production in the brain [51], where it is involved to the activation of diverse cellular second messenger cascades [52,53], including the regulation of OPC migration and differentiation following brain injury [54]. Histological examination revealed a significantly increased density of $GFAP^+$ astrocytes within the corpus callosum of $RIT1^{KO}$ mice, relative to WT controls ($n = 4$, $p < 0.01$) (Fig. 9). Taken together, these data demonstrate that *RIT1* loss is correlated with an increase in the number of astrocytes within the CC and ET-1 expression in the brain.

3. Discussion

Our study provides insight into the cellular and behavioral processes affected by the RIT1 GTPase. Using our one-of-a-kind global *RIT1* knockout mouse model [35], we provide *in vivo* evidence that RIT1 plays an important role(s) in the control of cerebral lipid levels, resulting in robust region-specific lipid changes. We also detected a selective reduction in the density of OLs, but an increased density of $GFAP^+$ glia, in the corpus callosum of $RIT1^{KO}$ mice, without changes to these cell populations in grey matter. The differences to select oligodendroglia subtypes was correlated with decreased levels of key myelin structural proteins, reduced conduction velocity in CC axonal tracts, and significant differences in locomotor ability and anxiety. These data establish an unexpected role for RIT1 signaling in the control of lipid metabolism, and show that $RIT1^{KO}$ mice display altered white matter tract oligodendroglial, reduced conduction velocity, and impaired basal behavioral measures of anxiety and locomotion.

The mammalian brain is highly enriched in heterogeneous lipids, where they play important roles as structural and signaling molecules. Lipids contribute to the structural integrity of cell and organelle membranes, control cellular signaling pathways, and regulate gene expression, neurogenesis, and neural communication [55,56]. The use of quantitative mass spectrometry-based lipidomic analysis first suggested widespread CNS lipid alterations in $RIT1^{KO}$ mice. These results were further buttressed by state-of-the-art MALDI-MSI analysis, permitting high-resolution spatial resolution of a more limited set of lipid species, and together demonstrate that *RIT1* loss results in complex alterations in the abundance and spatial distribution of a diverse array of lipid species within the mouse brain. Notable changes included a significant reduction in glycosphingolipids (GSLs) and sulfated

galactocerebrosides, sulfatides, which are major lipid components of myelin [44] within the corpus callosum, suggesting that impaired lipid biosynthesis resulting from *RIT1* deletion may compromise myelin integrity. Indeed, LFB staining was significantly reduced in the CNS of *RIT1*^{KO} mice, including a quantitative reduction in staining within the corpus callosum, further supporting a role for *RIT1* signaling in maintaining myelin levels and myelinated axons within the corpus callosum (Fig. 3D). However, alterations in lipid levels within the brain of *RIT1*^{KO} mice have implications beyond myelination. Transcriptional differences in lipid metabolic genes have been noted between quiescent and activated NSCs [39,57], with fatty acid oxidation being required for NSC proliferation [58,59], and lipid metabolic defects serving to disrupt NSC proliferation [40]. Interesting, the MALDI-MSI data suggests that fatty acid levels in the hippocampus of *RIT1*^{KO} mice are reduced (Fig. 1B; see *m/z* 255, 279, and 281). Additional studies are needed to determine whether modulation of CNS lipids contributes to *RIT1*^{KO}-dependent regulation of hippocampal neurogenesis following contusive brain injury, exercise stimulus, and/or IGF-1 signaling [34,37,38].

The reduction in myelin-associated lipids within the corpus callosum of *RIT1*^{KO} mice detected by MALDI-MSI (Fig. 3) motivated our analysis of oligodendrogenesis, as a central function of OLs is to generate and maintain myelin. Immunohistochemical staining found clear regional differences in mature OL numbers (Figs. 4 and 5), with the corpus callosum of *RIT1*^{KO} mice displaying a significantly reduced density of OLs, while oligodendrocyte numbers were not noticeably altered in the cortex of *RIT1*^{KO} mice relative to wild-type controls. *RIT1* [60] is widely expressed within the CNS, including astrocytes, neurons, OPCs and myelinating oligodendrocytes. Thus, *RIT1* loss may both directly impact intrinsic oligodendrocyte cellular signaling cascades, and indirectly impact the complex regulatory network involved in the control of OL maturation, migration and myelination by altering critical extrinsic factors [1,2,7]. Previous studies have found that *RIT1* modulates hippocampal neurogenesis via regulation of an Akt-Sox2 signaling cascade [37,38], and that RIT1-dependent survival signaling relies on mTORC2 signal transduction [61]. Importantly, these signaling pathways also play critical roles in the control of OL survival, migration, differentiation, and myelination. Constitutive activation of PI3K/Akt signaling in OPCs/OLs has been shown to enhance myelin formation without altering OL generation [62–64], while inhibition of the downstream effector mTOR results in defective OL differentiation [65,66]. Sox2-dependent transcription appears to play complex roles in oligodendroglia, including region-specific roles in the regulation of OPC proliferation, OL differentiation, and myelination [67–69]. Finally, RIT1 loss is associated with reduced SIRT1 expression (Fig. 8B), which is known to regulate both lipid metabolism but can also influence OPC proliferation and differentiation [70]. Additional studies will be needed to examine the potential contribution of RIT1 to the control of these signaling cascades in oligodendroglial differentiation and physiology.

In a screen to identify genes involved in lipid metabolism impacted by *RIT1* loss, the expression of several genes were found to be changed, including perilipin-2 [71], SIRT1 [72], and angiopoietin-like 4 [73], that have previously been implicated in myelination. Studies are underway to define their roles in RIT1 control of cerebral lipid levels and myelin. The screen also identified ET-1, whose protein levels were found to be significantly upregulated in *RIT1*^{KO} animals (Fig. 8). Astrocytes are largely responsible for ET-1 production in the brain [51], and elevated ET-1 levels have been found to affect oligodendrocyte differentiation [51,54]. *RIT1*^{KO} animals express increased GFAP^{+} astrocyte numbers in the CC (Fig. 9), suggesting that these cells might generate locally elevated ET-1 levels. While increased ET-1 levels would be consistent with the reduction in OLs observed in the corpus callosum of *RIT1*^{KO} mice, we would predict this decrease to be accompanied by an increase in immature oligodendrocyte precursor cells [74]. However, total oligodendroglial cell numbers were reduced, suggesting that the impact of *RIT1* loss on OLs levels in the CC are not solely driven by altered ET-1 signaling. Studies are ongoing to determine how ET-1 signaling might contribute to the alterations in OL numbers and lipid metabolism observed in *RIT1*^{KO} animals.

Perturbations in lipid metabolism and defects in OL differentiation are known to impede myelination [2,13,14,75]. Consistent with a role for RIT1 in moderating myelination, *RIT1*^{KO} mice display a significant reduction in the expression of the myelin-specific proteins MBP, MAG, and CNPase (Fig. 3F) and in the staining of myelin and myelinated axons by Luxol Fast Blue (Fig. 3D). However, there was no change in the thickness of the mutant corpus callosum relative to wild-type controls (Fig. 3E). Alterations in myelin lipid biosynthesis have previously been shown to distort the stoichiometry of myelin proteins and result in changes to the structure of myelin sheaths [2,13,76,77], and have been found to correlate with slower conduction velocities [2,78,79]. Indeed, either a reduction in axonal myelination [78,80], alternations in the expression of distinct myelin proteins [80,81], or changes in myelin lipids [76,82,83] can produce slowed axonal conductance velocity. Our data demonstrate that *RIT1* loss results in a significant reduction in axonal conduction velocity within the CC. Genetic ablation of oligodendrogenesis in the adult brain results in a decrease in conduction velocity in the corpus callosum and progressive motor deficits [75]. In keeping with a mild myelination defect, *RIT1*^{KO} mice displayed modest deficits in locomotor performance (Fig. 7) but do not develop the spontaneous epilepsy or aberrant coordinated movements observed in many mouse models of myelinopathy [48,84]. While altered myelination may underlie the reduction in conduction velocity, previous work has described *RIT1* as a regulator of neural stems cells, neurogenesis, and both axonal and dendritic morphology [29,34], with altered neuronal function certainly capable of impacting conduction velocity and behavior. Thus, studies are needed to understand the direct impact of RIT1 activity in oligodendrocytes, especially to myelination, or whether this is an epiphenomenon arising from altered neuronal function changing signaling to OLs and thereby influencing myelination. In addition, it is important to define the primacy of *RIT1*^{KO}-dependent lipid metabolic alterations to myelin stabilization. Addressing these open questions is currently hampered by the lack of a conditional *RIT1* knockout mouse model to more fully address the physiological role(s) of neuronal and oligodendroglial *RIT1* activity.

In summary, here we identify RIT1 as a regulator of cerebral lipid metabolism, with *RIT1* deficiency correlated with altered white matter oligodendrocyte lineage cells and myelin-associated protein expression within the CNS. Based on these results, we suggest that the role of RIT1 in demyelinating diseases should be examined, as the failure to maintain OL numbers and inappropriate myelin lipid levels represent major causes of myelinopathies and defective remyelination. Presumably, modulation of RIT1 activity might represent a potential therapeutic strategy to combat various demyelination disorders.

4. Limitations of the study

In this study we identified RIT1 as a regulator of lipid metabolism in the brain, using a global *RIT1* knockout mouse model. As RIT1 is widely expressed, including in diverse cell types within the brain, further investigation of potential cell-type specific contributions to lipid metabolism is needed. We find changes to white matter oligodendrocyte lineage cells, and significant reductions in myelin-associated proteins and general myelin staining in RIT1 null mice. Defects in lipid biosynthesis have previously been shown to distort the stoichiometry of myelin proteins, result in changes to the structure of myelin sheaths, and to correlate with slower axonal conduction velocities. As RIT1 is known to impact neuronal development, neural morphology, and signaling, additional studies are needed to determine if these differences are a direct result of altered RIT1 activity in oligodendrocytes, especially to myelination, or whether this is an epiphenomenon arising from altered neuronal function, resulting in changes in neuron-OL signaling. The MALDI-MSI method here provides an unprecedented anatomic resolution. However, the mass-unit resolution of the instrument limits the unambiguous identification of many lipid species, limiting the range of lipids that can be examined.

5. STAR methods

5.1. Animals

The generation and genotyping strategy for $RIT1^{KO}$ mice have previously been described [35]. Genotyping of offspring was performed by PCR using genomic DNA from tail biopsies. Adult mice (3–4 months of age) were housed in a climate-controlled environment with a 14/10 h light/dark cycle with solid diet and water provide ad libitum throughout the study. The Institutional Animal Care and Use Committee of the University of Kentucky approved all the animal procedures carried out in this study under PHS Assurance #A3336-01.

5.2. Reagents

High-performance liquid chromatography (HPLC)-methanol, and HPLC-grade water were obtained from Sigma-Aldrich. alpha-cyano-4-hydroxycinnamic acid (CHCA) was obtained from Caymen Chemical. Luxol Fast Blue (LFB) was obtained from Acros Organics.

5.2.1. Tissue collection and processing

Mice were euthanized by cervical dislocation for metabolic analysis, and brains were immediately removed and placed in liquid nitrogen. Whole brains were then pulverized to 5-μm particles in liquid nitrogen using a Freezer/Mill® cryogenic grinder (SPEX SamplePrep model 6875D) [85,86]. Pulverized tissues were stored at liquid nitrogen for further RNA, protein and metabolomics analysis. For histology analysis, mice were deeply anesthetized with Fetal-plus (65 mg/kg intraperitoneal sodium pentobarbital) and perfused with heparinized saline followed by 4% paraformaldehyde. Brains were removed from the skull immediately and post-fixed in 4% paraformaldehyde at 4 °C overnight, and cryoprotected in 30% sucrose for up to 48h. Fully immersed brains were finally embedded in Tissue-Tek optimal cutting compound (Sakura Finetek, USA), snap-frozen on dry ice cooled isopentane. Coronal brain cryosections (15 μm: Bregma level −2.03 mm) were cut with a Leica CM1860 cryostat and collected on Superfrost Plus slides (VWR).

5.2.2. Lipotype analysis

Whole brains were pulverized to 5-μm particles in liquid nitrogen using a Freezer/Mill® cryogenic grinder [85]. Cryomilled brain tissue (5 mg) was homogenized in 1 ml D-PBS (without Mg^{2+}, Ca^{2+}). Homogenized samples (5 mg/ml) were used for lipidomic analysis performed by Lipotype GmbH (Dresden, Germany). Lipidomic data was analyzed to class-specific internal standards, enabling the detection of 133 unique lipid specifics of 10 analyzed classes. The distribution of lipids was further analyzed using MetaboAnalyst 5.0 online software (https://www.metaboanalyst.ca/).

Lipid extraction for mass spectrometry lipidomics.

Mass spectrometry-based lipid analysis was performed at Lipotype GmbH (Dresden, Germany) as described [87]. Lipids were extracted using a chloroform/methanol procedure [88]. Samples were spiked with internal lipid standard mixture containing: diacylglycerol 17:0/17:0 (DAG), phosphatidate 17:0/17:0 (PA), phosphatidylcholine 17:0/17:0 (PC), phosphatidylethanolamine 17:0/17:0 (PE), phosphatidylglycerol 17:0/17:0 (PG), phosphatidylinositol 16:0/16:0 (PI), phosphatidylserine 17:0/17:0 (PS), cholesterol ester 20:0 (CE), sphingomyelin 18:1; 2/12:0; 0 (SM) and triacylglycerol 17:0/17:0/17:0 (TAG). After extraction, the organic phase was transferred to an infusion plate and dried in a speed vacuum concentrator. The dry extract was re-suspended in 7.5 mM ammonium acetate in chloroform/methanol/propanol (1:2:4, V:V:V) and in 33% ethanol solution of methylamine in chloroform/methanol (0.003:5:1; V:V:V). All liquid handling steps were performed using Hamilton Robotics STARlet robotic platform with the Anti Droplet Control feature for organic solvents pipetting.

MS data acquisition.

Samples were analyzed by direct infusion on a QExactive mass spectrometer (Thermo Scientific) equipped with a TriVersa NanoMate ion source (Advion Biosciences). Samples were analyzed in both positive and negative ion modes (collision energy: positive mode: 20%; negative mode: 35%) with a resolution of $R_{m/z\,=\,200} = 280000$ for MS and $R_{m/z\,=\,200} = 17500$ for MSMS experiments, in a single acquisition. MSMS was triggered by an inclusion list encompassing corresponding MS mass ranges scanned in 1 Da increments [42]. Both MS and MSMS data were combined to monitor CE, DAG and TAG ions as ammonium adducts; PC as acetate adduct; and PA,

PE, PG, PI and PS as deprotonated anions. MS only was used to monitor SM as acetate adduct.

5.3. MS data analysis and post-processing

Data were analyzed by Lipotype with in-house developed lipid identification software based on LipidXplorer [89,90]. Data post-processing and normalization were performed using an in-house developed data management system. Only lipid identifications with a signal-to-noise ratio >5, and a signal intensity 5-fold higher than in corresponding blank samples were considered for further data analysis.

5.3.1. Tissue preparation for MALDI-MSI

Mice were sacrificed by cervical dislocation followed by immediate brain extraction and preservation as described in Stanback et al. [91]. Briefly, a bath of isopentane was prepared over dry ice. An aluminum foil weigh boat was floated on the bath and brain tissue was allowed to gradually freeze for 7 min (to preserve tissue structure). The brain was then placed in an additional aluminum foil packet, dropped into liquid nitrogen and stored until sectioning. Using a cryostat, brain slices were sectioned at 10 μm on charged slides and stored at −80 °C.

5.3.2. Slide preparation for MALDI-MSI

After desiccation for 1 h, slides were sprayed with 10 passes of 7 mg/mL CHCA matrix (alpha-cyano-4-hydroxycinnamic acid (CHCA), Caymen Chemical) in 50% acetonitrile/0.1% TFA, applied at 0.1 mL/min with a 2.5 mm offset and a velocity of 1300 at 79 °C and 10psi using the M5 Sprayer. Slides were used immediately or stored in a desiccator until analysis.

MALDI-MSI.

For the detection of lipids, a Waters SynaptG2-Xs high-definition mass spectrometer equipped with traveling wave ion mobility was used. The laser was operated at 1000 Hz with an energy of 200 AU and spot size of 50 μm at X and Y coordinates of 100 μm with mass range set at 50–2000 *m/z* in negative mode. Once collected, spectra were uploaded to High Definition Imaging (HDI) Software (Waters Corporation) to allow for the generation of lipid images. Regions of interest (ROIs) were defined by comparison to an H&E stained adjacent slide, highlighting the structural components of the brain. Mass assignments were made through accurate mass and previously published annotations [92,93]. H&E slides were scanned and exported using HALO™ software. ▣For all pixels defined within a ROI, peak intensities were averaged and normalized by total ion current.

5.3.3. Immunoblotting

Cryomilled tissues [85] were homogenized using a Tissue Dounce grinder (Thomas Scientific) on ice in lysis buffer (20 mM Tris·HCl pH 7.5, 250 mM NaCl, 10 mM $MgCl_2$, 1% Triton X-100, 1 mM Na_3VO_4, 50 mM β-glycerophosphate, 1 × protease inhibitor cocktail (Roche)). Cleared whole cell lysates (14,000 rpm for 10 min) were generated, and protein concentration determined by the Bradford method (BioRad). Lysates were resolved by 12% SDS-PAGE, transferred to nitrocellulose membranes (2h, 250 mA), and subjected to immunoblotting with the following antibodies: endothelin 1 (1:1000 dilution, Fisher Scientific, MA3-005), Perilipin 2 (1:1000 dilution, Abcam, ab108323), MBP (myelin basic protein, 1:1000 dilution, Cell Signaling, 78896), CNPase (1:1000 dilution, Cell Signaling, 5664), MAG (myelin associated glycoprotein, 1:1000 dilution, Cell Signaling, 9043), and GAPDH (1:5000 dilution, Cell Signaling, 5174s). Membrane were developed by chemiluminescence (HyGlo, Denville Scientific) using a ChemiDoc MP with Image Lab software (BioRad).

Luxol fast blue (LFB) staining.

Paraformaldehyde-fixed, paraffin embedded, coronal brain sections from wild-type (WT) and *Rit1*^{KO} mice (5 μm) were processed together for Luxol Fast Blue (LFB) staining to detect myelin/myelinated axons [45]. Sections were deparaffinized in xylene, rehydrated in a gradient of ethanol solutions and incubated in LFB for 2 h at 60 °C. Post incubation, sections were briefly immersed in 0.05% lithium carbonate solution for differentiation and counterstained in Nissl stain. The sections were taken through a gradient of ethanol solutions and cleared in xylene before mounting in DPX (Sigma Aldrich). Sections were imaged using a Nikon Ti2 equipped with a DSRi2 color camera. The images were processed in ImageJ using the Color Deconvolution algorithm to separate the Nissl from the LFB stain. The deconvolved LFB images were then analyzed using NIS Elements. A region of interest was outlined within the corpus callosum and a threshold was applied for the dark blue stain. Using the automated count feature of Elements, the area of the ROI and the sum density was generated for each section. A total of nine sections for each genotype were analyzed. The resulting density/mm2 were analyzed using GraphPad Prism.

5.3.4. Immunofluorescence Microscopy and automated cell counting

For immunofluorescence analysis, sections were washed with 1xPBS 3 times (5 min/each wash) and incubated with blocking and permeabilizing buffer (5% normal goat serum and 0.1% Triton X-100 in 1xPBS) with gentle agitation for 30 min at RT. For immunohistochemistry analysis, sections underwent general antigen retrieval using citrate buffer. Sections were washed with 1x PBS and incubated with blocking buffer (5% normal goat serum and 0.1% Triton X-100 in 1x PBS) for 30min, RT. Primary antibodies against olig2 (1:500 dilution, Fisher Scientific, NBP128667), CC1 (1:200 dilution, Abcam, ab16794), MBP (1:250 dilution, Abcam, ab7349), GFAP (1:1000 dilution, Dako, Z0334) and cleaved Caspase 3 (1:1600, Cell Signaling Technology, 9664) were diluted in blocking buffer and incubated with sections overnight at 4 °C, followed by extensive washing with 1x PBS at RT. Then secondary antibodies, either conjugated with Alexa 488 or Alexa 594 (1:500 dilution, Jackson ImmunoResearch Laboratory Inc.) were applied to the sections for at least 1 h at RT. The sections were washed and SlowFade Gold antifade mounting medium with DAPI (Invitrogen) was applied prior to

adhering coverslips. Imaging was performed using a Nikon Ti2 microscope equipped with a DS-Ri2 color camera or a Nikon A1R confocal microscope.

NIS Elements software was used for automated cell counting. Confocal micrographs were collected of the cortex and corpus callosum. Briefly, the Analysis Explorer module of Elements was used to define binary layers overlapping the fluorescent signal for DAPI, olig2 and CC1 by setting thresholds for both fluorescent signal and object size. Once the parameters were set and were validated for both genotypes, the entire set of images was set up for batch counting of the positive with limitations that the olig2 and CC1 staining must overlap with DAPI staining to be counted as a cell. The entire field was used for the cortex. For the corpus callosum, a region of interest (ROI) was manually drawn around the corpus callosum based on a DIC image of the same area and only the cells within the ROI were analyzed. A similar process was followed for the astrocyte counts with thresholds set for DAPI and GFAP.

5.3.5. Lipid metabolism PCR assay and quantitative real-time PCR

Lipid metabolism Tier 1 M96 PCR plates (BioRad, 10029231) were used for to screen for altered expression of genes involved in lipid metabolism from WT and RIT1 knockout mouse brains. Briefly, total RNA was isolated from pulverized brain tissues (n = 3 each group) by using Aurum Total RNA Mini Kit (BioRad, 7326820). 1 μg total RNA was reverse-transcribed using a Bio-Rad RT kit. The cDNA was diluted 1:5 in ultrapure water for final PCR. The cDNA was mixed with SYBR Green into the array plates, and cycling was performed with BioRad CFX 96 Real Time System according to the instructions of the manufacturer. The values were obtained using the 2-ΔΔCT method and plotted as heatmap. To independently verify the gene expression changes observed in the PCR plate assay, new total brain mRNA was isolated (n = 3 additional mice per group), reverse-transcribed (1 μg) using a BioRad RT kit, and assayed by QPCR using a BioRad CFX 96 Real Time System. Primers used were: Endothelin 1 (primer pairs: 5′- GCACCGGAGCTGAGAATGG-3’; 5′- GTGGCAGAAGTAGACACACTC-3′); Perilipin 2 (primer pairs: 5′- GACCTTGTGTCCTCCGCTTAT-3’; 5′- CAACCGCAATTTGTGGCTC-3′); PRKCD (primer pairs: 5′- CCTCCTGTACGAAATGCTCATC-3’; 5′- GTTTCCTGTTACTCCCAGCCT-3′); Phospholipase A2 Group IVA (PLA2G4A, primer pairs: 5′- CAGCACATTATAGTGGAACACCA-3’; 5′- AGTGTCCAGCATATCGCCAAA-3′); Peroxisome Proliferator Activated Receptor Delta (PPARD, primer pairs: 5′- TCCATCGTCAACAAAGACGGG-3’; 5′- ACTTGGGCTCAATGATGT CAC-3′); TBP (primer pairs:5′- CTACCGTGAATCTTGGCTGTAAAC-3’; 5′- AATCAACGC AGTTGTCCG TGGC-3′).

5.3.6. Electrophysiological recordings of nerve conduction velocity (N1 and N2) responses

N1 and N2 responses were recorded in coronal slices (1–4 per animal) obtained from a total of 10 animals (n = 5 per group). Briefly, WT and $RIT1^{KO}$ mice were first anesthetized (3% isoflurane) before decapitation. Brains were then extracted and placed into ice-cold, oxygenated (95% O_2, 5% CO_2) low $CaCl_2$, high $MgCl_2$ (0.1 mM $CaCl_2$, 8 mM $MgCl_2$) artificial cerebrospinal fluid (ACSF; [in mM] 114 NaCl, 3 KCl, 1.25 KH_2PO_4, 26 $NaHCO_3$, 10 D-glucose) for ~10 min. Coronal slices (~400 μm thick) centered on Bregma (±800 μm) and containing the corpus callosum (CC) were cut using a McIlwain Tissue Chopper. Slices were transferred to an interface-type recording chamber, maintained in oxygenated normal $CaCl_2$ and $MgCl_2$ (2.5 mM $CaCl_2$, 1.3 mM $MgCl_2$) recording ACSF, and allowed to incubate for ~1.5 h. All recordings of N1 and N2 responses were accomplished at room temperature using low-resistance electrodes (2–3 MΩ) pulled on an electrode puller (P-87 Flaming/Brown Micropipette Puller, Sutter Instrument Co., Novato, CA) and filled with recording ACSF. Using a dissecting microscope mounted above the recording chamber, a twisted bipolar stainless-steel stimulating electrode (0.0045 in, coated; A-M Systems Inc., Everett, WA) was positioned near the midline in the CC. The recording electrode was then placed ~0.75 mm laterally and the slices were stimulated using a SD9K stimulator (Astro Med Inc., Grass Instruments, Warwick, RI). Input–output (*I/O*) relationships were recorded and used to determine the maximum response for each slice. Field EPSPs (fEPSPs) were then obtained using a stimulation at 0.033 Hz with an intensity set to 50% of the maximum response of that slice. fEPSP responses were averaged (6–7 traces per slice) and analyzed using Clampex 11 (pCLAMP 11 Software Suite, Molecular Devices LLC, San Jose, CA) and AxoGraph X (AxoGraph Scientific, Berkley, CA) to derive measures of N1 and N2 response delay, conductance velocity, amplitude peak, amplitude slope, rise time, and half-width. Prior to all statistical comparisons, all slices taken from the same animal were averaged to derive a single data point per animal for each measure tested; thus, for this phase of the study, each n represents a single animal.

5.3.7. Behavior analysis

All behavior experiments were performed with the Mouse Behavioral Core at the University of Kentucky. The experimenter was blinded to the mouse genotype during animal testing and data analysis. All tests were monitored by a digital video camera and analyzed in a blinded manner. For each test, the analysis was performed each day at the same time during light cycle. Mice were acclimated in the testing room for at least 30 min prior to testing.

Open field: The open field chamber monitors locomotion, exploration, anxiety, and risk assessment in response to a novel environment [94]. Mice were placed in the middle of the open field apparatus which consisted of square box (50 × 50 cm) with illumination (30 lux), and were given 15 min to explore. Time in the center and crossing center frequencies were recorded and analyzed using EthoVision software (Noldus information technology).

Rotarod: The rotarod test was used to assess the mice motor function and balance [95]. Mice were placed on a four-lane rotarod device (San Diego instruments, San Diego, CA, USA), and the latency to fall from the accelerating rotarod was recorded. To help ensure a basic level of performance, each mouse underwent three rounds of training, each lasting for 60 s at 4 rpm, with a 30 min interval between training periods. Following training, mice were placed on a rotarod set on the 1–40 rpm accelerating mode over 90 s. Each trial ran for a maximum of 300 s. Trials ended when mice either fell off the rod or clung to the rod as it made three complete rotations. Mice underwent three sessions of training and testing with a 30 min interval between trials. Individual scores from three tests were averaged and evaluated to assess motor function.

Four–limb hanging test: The four-limb hanging test was used to evaluate limb strength and is based on the tendency of a mouse to grasp a grid when suspended [96]. Mice were placed on the cage top, which was then inverted, and the time the animal remained suspended was recorded. Each trial ran for a maximum of 500 s. Mice underwent three trials with a 30 min interval between tests for three consecutive days. Individual scores from the nine tests were averaged to assess grip strength.

5.4. Statistical analysis

Statistical analyses were carried out using GraphPad Prism 9.0 and Metaboanalyst 5.0. For Metaboanalyst multivariate analyses log transformation and auto scaling were used to normalization. Heatmaps were generated based on the Euclidean distance measure and the Ward clustering algorithm. Lipids/genes with variable importance in projection (VIP) scores >1.5 based on partial least squares discrimination analysis (PLS-DA) were selected for further analysis. Data was uploaded as a.csv file and auto-scaled (mean-centered and divided by the standard deviation of each variable) using the top features ranked by PLS-DA, VIP, and distance measured by a Euclidean analysis. For univariate analysis of individual lipids/genes, all numerical data were analyzed using GraphPad Prism 9.0 and are presented as mean ± SEM. Statistical analysis of protein expression and tissue cell counting was performed using an unpaired, 2-tailed *t*-test or one-way ANOVA with post hoc analysis using Tukey-Kramer multiple comparisons. Three technical replicates for each tissue (three biological replicates) were averaged. Student's t-tests (two-tailed, unpaired, equal variance) were used to compare genotype groups for all electrophysiological measures assessed. Statistical significance was set at $p < 0.05$.

Author contribution statement

Lei Wu: Conceived and designed the experiments; Performed the experiments; Analyzed and interpreted the data. </p>

Fang Wang, Carole L. Moncman, Mritunjay Pandey, Hilaree N. Frazier, Lyndsay E.A. Young: Performed the experiments; Analyzed and interpreted the data. </p>

Harrison A. Clarke: Performed the experiments. </p>;

Matthew S. Gentry: Contributed reagents, materials, analysis tools or data. </p>

Weikang Cai: Conceived and designed the experiments; Analyzed and interpreted the data; Contributed reagents, materials, analysis tools or data. </p>;

Olivier Thibault: Conceived and designed the experiments; Performed the experiments; Analyzed and interpreted the data; Wrote the paper. </p>

Ramon C. Sun: Conceived and designed the experiments; Analyzed and interpreted the data; Contributed reagents, materials, analysis tools or data; Wrote the paper. </p>

Douglas A. Andres: Conceived and designed the experiments; Analyzed and interpreted the data; Wrote the paper. </p>

Data availability statement

Data will be made available on request.

Declaration of competing interest

Ramon C. Sun has received research support and has received a consultancy fee from Maze Therapeutics. Matthew S. Gentry has received research support and research compounds from Maze Therapeutics, Valerion Therapeutics, and Ionis Pharmaceuticals. Matthew S. Gentry also received a consultancy fee from Maze Therapeutics, PTC Therapeutics, and the Glut1-Deficiency Syndrome Foundation. Fang Wang, Lei Wu, Mritunjay Pandey, Harrison A. Clarke, Hilaree N. Frazier, Carole L. Moncman, Weikang Cai, Lyndsay E.A. Young, Olivier Thibault, and Douglas A. Andres report no disclosures.

The content is the responsibility of the authors and does not necessarily represent the official views of the NIH. The paper is subject to the NIH Public Access Policy. This study was carried out in accordance with the Uniform Requirements for Manuscripts Submitted to Biomedical Journals.

Acknowledgements

We would like to Mrs. Dana Napier for performing immunohistochemical-staining on tissue slices at the Markey Cancer Center. This work was supported by National Institutes of Health (NIH) grants R01 NS102196, R56NS124707 and Kentucky Spinal Cord and Head Injury Trust grant 16-1 awarded to Douglas A. Andres, NIH grant R01 MH125903 to Weikang Cai, NIH grant R01 AG033649 to Olivier Thibault, NIH grants R35 NS116824 and P01 NS097197 to Matthew S. Gentry, Hilaree N. Frazier was supported by NIH/NIA training grant T32AG057461, and Lyndsay E. A. Young was support by NIH/NCI F99CA2664165. This research was also supported by funding from the University of Kentucky Markey Cancer Center and the NIH-funded Biospecimen Procurement & Translational Pathology Shared Resource Facility of the University of Kentucky Markey Cancer Center P30 CA177558.

Appendix A. Supplementary data

Supplementary data related to this article can be found at https://doi.org/10.1016/j.heliyon.2023.e20384.

References

[1] A.L. Herbert, K.R. Monk, Advances in myelinating glial cell development, Curr. Opin. Neurobiol. 42 (2017) 53–60, https://doi.org/10.1016/j.conb.2016.11.003.

[2] K.A. Nave, H.B. Werner, Myelination of the nervous system: mechanisms and functions, Annu. Rev. Cell Dev. Biol. 30 (2014) 503–533, https://doi.org/10.1146/annurev-cellbio-100913-013101.

[3] N. Baumann, D. Pham-Dinh, Biology of oligodendrocyte and myelin in the mammalian central nervous system, Physiol. Rev. 81 (2001) 871–927, https://doi.org/10.1152/physrev.2001.81.2.871.

[4] U. Funfschilling, L.M. Supplie, D. Mahad, S. Boretius, A.S. Saab, J. Edgar, B.G. Brinkmann, C.M. Kassmann, I.D. Tzvetanova, W. Mobius, et al., Glycolytic oligodendrocytes maintain myelin and long-term axonal integrity, Nature 485 (2012) 517–521, https://doi.org/10.1038/nature11007.

[5] Y. Lee, B.M. Morrison, Y. Li, S. Lengacher, M.H. Farah, P.N. Hoffman, Y. Liu, A. Tsingalia, L. Jin, P.W. Zhang, et al., Oligodendroglia metabolically support axons and contribute to neurodegeneration, Nature 487 (2012) 443–448, https://doi.org/10.1038/nature11314.

[6] C. Stadelmann, S. Timmler, A. Barrantes-Freer, M. Simons, Myelin in the central nervous system: structure, function, and Pathology, Physiol. Rev. 99 (2019) 1381–1431, https://doi.org/10.1152/physrev.00031.2018.

[7] C. Taveggia, M.L. Feltri, L. Wrabetz, Signals to promote myelin formation and repair, Nat. Rev. Neurol. 6 (2010) 276–287, https://doi.org/10.1038/nrneurol.2010.37.

[8] C.B. Chan, X. Liu, L. Zhao, G. Liu, C.W. Lee, Y. Feng, K. Ye, PIKE is essential for oligodendroglia development and CNS myelination, Proc Natl Acad Sci U S A 111 (2014) 1993–1998, https://doi.org/10.1073/pnas.1318185111.

[9] M. Sanz-Rodriguez, A. Gruart, J. Escudero-Ramirez, F. de Castro, J.M. Delgado-Garcia, F. Wandosell, B. Cubelos, R-Ras1 and R-ras2 are essential for oligodendrocyte differentiation and survival for correct myelination in the central nervous system, J. Neurosci. 38 (2018) 5096–5110, https://doi.org/10.1523/JNEUROSCI.3364-17.2018.

[10] J.F. Silva-Rodrigues, C.F. Patricio-Rodrigues, V. de Sousa-Xavier, P.M. Augusto, A.C. Fernandes, A.R. Farinho, J.P. Martins, R.O. Teodoro, Peripheral axonal ensheathment is regulated by RalA GTPase and the exocyst complex, Development 147 (2020), https://doi.org/10.1242/dev.174540.

[11] T. Thurnherr, Y. Benninger, X. Wu, A. Chrostek, S.M. Krause, K.A. Nave, R.J. Franklin, C. Brakebusch, U. Suter, J.B. Relvas, Cdc42 and Rac1 signaling are both required for and act synergistically in the correct formation of myelin sheaths in the CNS, J. Neurosci. 26 (2006) 10110–10119, https://doi.org/10.1523/JNEUROSCI.2158-06.2006.

[12] Y. Zou, W. Jiang, J. Wang, Z. Li, J. Zhang, J. Bu, J. Zou, L. Zhou, S. Yu, Y. Cui, et al., Oligodendrocyte precursor cell-intrinsic effect of Rheb1 controls differentiation and mediates mTORC1-dependent myelination in brain, J. Neurosci. 34 (2014) 15764–15778, https://doi.org/10.1523/JNEUROSCI.2267-14.2014.

[13] R. Chrast, G. Saher, K.A. Nave, M.H. Verheijen, Lipid metabolism in myelinating glial cells: lessons from human inherited disorders and mouse models, J. Lipid Res. 52 (2011) 419–434, https://doi.org/10.1194/jlr.R009761.

[14] S. Schmitt, L.C. Castelvetri, M. Simons, Metabolism and functions of lipids in myelin, Biochim. Biophys. Acta 1851 (2015) 999–1005, https://doi.org/10.1016/j.bbalip.2014.12.016.

[15] J.S. O'Brien, Stability of the myelin membrane, Science 147 (1965) 1099–1107, https://doi.org/10.1126/science.147.3662.1099.

[16] A. Raasakka, P. Kursula, Flexible players within the sheaths, The Intrinsically Disordered Proteins of Myelin in Health and Disease. Cells 9 (2020), https://doi.org/10.3390/cells9020470.

[17] J. Colicelli, Human RAS superfamily proteins and related GTPases, Sci. STKE 2004 (2004) RE13.

[18] J. Cherfils, M. Zeghouf, Regulation of small GTPases by GEFs, GAPs, and GDIs, Physiol. Rev. 93 (2013) 269–309, https://doi.org/10.1152/physrev.00003.2012.

[19] A.D. Cox, C.J. Der, Ras history: the saga continues, Small GTPases 1 (2010) 2–27, https://doi.org/10.4161/sgtp.1.1.12178.

[20] K.A. Rauen, The RASopathies, Annu Rev Genomics Hum Genet 14 (2013) 355–369, https://doi.org/10.1146/annurev-genom-091212-153523.

[21] G.X. Shi, W. Cai, D.A. Andres, Rit subfamily small GTPases: regulators in neuronal differentiation and survival, Cell. Signal. 25 (2013) 2060–2068, https://doi.org/10.1016/j.cellsig.2013.06.002.

[22] R. Van, A. Cuevas-Navarro, P. Castel, F. McCormick, The molecular functions of RIT1 and its contribution to human disease, Biochem. J. 477 (2020) 2755–2770, https://doi.org/10.1042/BCJ20200442.

[23] Y. Aoki, T. Niihori, T. Banjo, N. Okamoto, S. Mizuno, K. Kurosawa, T. Ogata, F. Takada, M. Yano, T. Ando, et al., Gain-of-function mutations in RIT1 cause Noonan syndrome, a RAS/MAPK pathway syndrome, Am. J. Hum. Genet. 93 (2013) 173–180, https://doi.org/10.1016/j.ajhg.2013.05.021.

[24] A.H. Berger, M. Imielinski, F. Duke, J. Wala, N. Kaplan, G.X. Shi, D.A. Andres, M. Meyerson, Oncogenic RIT1 mutations in lung adenocarcinoma, Oncogene 33 (2014) 4418–4423, https://doi.org/10.1038/onc.2013.581.

[25] M. Koenighofer, C.Y. Hung, J.L. McCauley, J. Dallman, E.J. Back, I. Mihalek, K.W. Gripp, K. Sol-Church, P. Rusconi, Z. Zhang, et al., Mutations in RIT1 cause Noonan syndrome - additional functional evidence and expanding the clinical phenotype, Clin. Genet. 89 (2016) 359–366, https://doi.org/10.1111/cge.12608.

[26] A. Vichas, A.K. Riley, N.T. Nkinsi, S. Kamlapurkar, P.C.R. Parrish, A. Lo, F. Duke, J. Chen, I. Fung, J. Watson, et al., Integrative oncogene-dependency mapping identifies RIT1 vulnerabilities and synergies in lung cancer, Nat. Commun. 12 (2021) 4789, https://doi.org/10.1038/s41467-021-24841-y.

[27] H. Cave, A. Caye, N. Ghedira, Y. Capri, N. Pouvreau, N. Fillot, A. Trimouille, C. Vignal, O. Fenneteau, Y. Alembik, et al., Mutations in RIT1 cause Noonan syndrome with possible juvenile myelomonocytic leukemia but are not involved in acute lymphoblastic leukemia, Eur. J. Hum. Genet. 24 (2016) 1124–1131, https://doi.org/10.1038/ejhg.2015.273.

[28] D.A. Andres, G.X. Shi, D. Bruun, C. Barnhart, P.J. Lein, Rit signaling contributes to interferon-gamma-induced dendritic retraction via p38 mitogen-activated protein kinase activation, J. Neurochem. 107 (2008) 1436–1447, https://doi.org/10.1111/j.1471-4159.2008.05708.x.

[29] P.J. Lein, X. Guo, G.X. Shi, M. Moholt-Siebert, D. Bruun, D.A. Andres, The novel GTPase Rit differentially regulates axonal and dendritic growth, J. Neurosci. 27 (2007) 4725–4736, https://doi.org/10.1523/JNEUROSCI.5633-06.2007.

[30] B. Antonny, P. Chardin, M. Roux, M. Chabre, GTP hydrolysis mechanisms in ras p21 and in the ras-GAP complex studied by fluorescence measurements on tryptophan mutants, Biochemistry 30 (1991) 8287–8295.

[31] G.X. Shi, D.A. Andres, Rit contributes to nerve growth factor-induced neuronal differentiation via activation of B-Raf-Extracellular signal-regulated kinase and p38 mitogen-activated protein kinase cascades, Mol. Cell Biol. 25 (2005) 830–846.

[32] G.X. Shi, W. Cai, D.A. Andres, Rit-mediated stress resistance involves a p38-mitogen- and stress-activated protein kinase 1 (MSK1)-dependent cAMP response element-binding protein (CREB) activation cascade, J. Biol. Chem. 287 (2012) 39859–39868, https://doi.org/10.1074/jbc.M112.384248.

[33] G.X. Shi, H. Rehmann, D.A. Andres, A novel cyclic AMP-dependent Epac-Rit signaling pathway contributes to PACAP38-mediated neuronal differentiation, Mol. Cell Biol. 26 (2006) 9136–9147, https://doi.org/10.1128/MCB.00332-06.

[34] W. Cai, S.W. Carlson, J.M. Brelsfoard, C.E. Mannon, C.L. Moncman, K.E. Saatman, D.A. Andres, Rit GTPase signaling promotes immature hippocampal neuronal survival, J. Neurosci. 32 (2012) 9887–9897, https://doi.org/10.1523/JNEUROSCI.0375-12.2012.

[35] W. Cai, J.L. Rudolph, S.M. Harrison, L. Jin, A.L. Frantz, D.A. Harrison, D.A. Andres, An evolutionarily conserved Rit GTPase-p38 MAPK signaling pathway mediates oxidative stress resistance, Mol. Biol. Cell 22 (2011) 3231–3241, https://doi.org/10.1091/mbc.E11-05-0400.

[36] W. Cai, J.L. Rudolph, T. Sengoku, D.A. Andres, Rit GTPase regulates a p38 MAPK-dependent neuronal survival pathway, Neurosci. Lett. 531 (2012) 125–130, https://doi.org/10.1016/j.neulet.2012.10.036.

[37] S. Mir, W. Cai, D.A. Andres, RIT1 GTPase regulates Sox2 transcriptional activity and hippocampal neurogenesis, J. Biol. Chem. 292 (2017) 2054–2064, https://doi.org/10.1074/jbc.M116.749770.

[38] S. Mir, W. Cai, S.W. Carlson, K.E. Saatman, D.A. Andres, IGF-1 mediated neurogenesis involves a novel RIT1/akt/sox2 cascade, Sci. Rep. 7 (2017) 3283, https://doi.org/10.1038/s41598-017-03641-9.

[39] P. Codega, V. Silva-Vargas, A. Paul, A.R. Maldonado-Soto, A.M. Deleo, E. Pastrana, F. Doetsch, Prospective identification and purification of quiescent adult neural stem cells from their in vivo niche, Neuron 82 (2014) 545–559, https://doi.org/10.1016/j.neuron.2014.02.039.

[40] M. Knobloch, S. Jessberger, Metabolism and neurogenesis, Curr. Opin. Neurobiol. 42 (2017) 45–52, https://doi.org/10.1016/j.conb.2016.11.006.
[41] S. Mir, D.A. Andres, Small GTPase RIT1 in mouse retina; cellular and functional analysis, Curr. Eye Res. 43 (2018) 1160–1168, https://doi.org/10.1080/02713683.2018.1482557.
[42] M.A. Surma, R. Herzog, A. Vasilj, C. Klose, N. Christinat, D. Morin-Rivron, K. Simons, M. Masoodi, J.L. Sampaio, An automated shotgun lipidomics platform for high throughput, comprehensive, and quantitative analysis of blood plasma intact lipids, Eur. J. Lipid Sci. Technol. 117 (2015) 1540–1549, https://doi.org/10.1002/ejlt.201500145.
[43] L. Montani, Lipids in regulating oligodendrocyte structure and function, Semin. Cell Dev. Biol. 112 (2021) 114–122, https://doi.org/10.1016/j.semcdb.2020.07.016.
[44] N. Jackman, A. Ishii, R. Bansal, Oligodendrocyte development and myelin biogenesis: parsing out the roles of glycosphingolipids, Physiology 24 (2009) 290–297, https://doi.org/10.1152/physiol.00016.2009.
[45] D.L. Yao, S. Komoly, Q.L. Zhang, H.D. Webster, Myelinated axons demonstrated in the CNS and PNS by anti-neurofilament immunoreactivity and Luxol fast blue counterstaining, Brain Pathol. 4 (1994) 97–100, https://doi.org/10.1111/j.1750-3639.1994.tb00815.x.
[46] S.P. Fancy, S.E. Baranzini, C. Zhao, D.I. Yuk, K.A. Irvine, S. Kaing, N. Sanai, R.J. Franklin, D.H. Rowitch, Dysregulation of the Wnt pathway inhibits timely myelination and remyelination in the mammalian CNS, Genes Dev. 23 (2009) 1571–1585, https://doi.org/10.1101/gad.1806309.
[47] R.G. Almeida, D.A. Lyons, On myelinated axon plasticity and neuronal circuit formation and function, J. Neurosci. 37 (2017) 10023–10034, https://doi.org/10.1523/JNEUROSCI.3185-16.2017.
[48] I. Griffiths, M. Klugmann, T. Anderson, D. Yool, C. Thomson, M.H. Schwab, A. Schneider, F. Zimmermann, M. McCulloch, N. Nadon, K.A. Nave, Axonal swellings and degeneration in mice lacking the major proteolipid of myelin, Science 280 (1998) 1610–1613, https://doi.org/10.1126/science.280.5369.1610.
[49] I.R. Griffiths, Myelin mutants: model systems for the study of normal and abnormal myelination, Bioessays 18 (1996) 789–797, https://doi.org/10.1002/bies.950181005.
[50] A. Ennaceur, Tests of unconditioned anxiety - pitfalls and disappointments, Physiol. Behav. 135 (2014) 55–71, https://doi.org/10.1016/j.physbeh.2014.05.032.
[51] A. Gadea, S. Schinelli, V. Gallo, Endothelin-1 regulates astrocyte proliferation and reactive gliosis via a JNK/c-Jun signaling pathway, J. Neurosci. 28 (2008) 2394–2408, https://doi.org/10.1523/JNEUROSCI.5652-07.2008.
[52] M.E. Lee, S.M. de la Monte, S.C. Ng, K.D. Bloch, T. Quertermous, Expression of the potent vasoconstrictor endothelin in the human central nervous system, J. Clin. Invest. 86 (1990) 141–147, https://doi.org/10.1172/JCI114677.
[53] V. Naidoo, S. Naidoo, R. Mahabeer, D.M. Raidoo, Cellular distribution of the endothelin system in the human brain, J. Chem. Neuroanat. 27 (2004) 87–98, https://doi.org/10.1016/j.jchemneu.2003.12.002.
[54] T.R. Hammond, B. McEllin, P.D. Morton, M. Raymond, J. Dupree, V. Gallo, Endothelin-B receptor activation in astrocytes regulates the rate of oligodendrocyte regeneration during remyelination, Cell Rep. 13 (2015) 2090–2097, https://doi.org/10.1016/j.celrep.2015.11.002.
[55] T. Harayama, H. Riezman, Understanding the diversity of membrane lipid composition, Nat. Rev. Mol. Cell Biol. 19 (2018) 281–296, https://doi.org/10.1038/nrm.2017.138.
[56] T. Shimizu, Lipid mediators in health and disease: enzymes and receptors as therapeutic targets for the regulation of immunity and inflammation, Annu. Rev. Pharmacol. Toxicol. 49 (2009) 123–150, https://doi.org/10.1146/annurev.pharmtox.011008.145616.
[57] D. Mizrak, H.M. Levitin, A.C. Delgado, V. Crotet, J. Yuan, Z. Chaker, V. Silva-Vargas, P.A. Sims, F. Doetsch, Single-cell analysis of regional differences in adult V-SVZ neural stem cell lineages, Cell Rep. 26 (2019) 394–406 e395, https://doi.org/10.1016/j.celrep.2018.12.044.
[58] K. Ito, T. Suda, Metabolic requirements for the maintenance of self-renewing stem cells, Nat. Rev. Mol. Cell Biol. 15 (2014) 243–256, https://doi.org/10.1038/nrm3772.
[59] M. Knobloch, S.M. Braun, L. Zurkirchen, C. von Schoultz, N. Zamboni, M.J. Arauzo-Bravo, W.J. Kovacs, O. Karalay, U. Suter, R.A. Machado, et al., Metabolic control of adult neural stem cell activity by Fasn-dependent lipogenesis, Nature 493 (2013) 226–230, https://doi.org/10.1038/nature11689.
[60] Y. Zhang, K. Chen, S.A. Sloan, M.L. Bennett, A.R. Scholze, S. O'Keeffe, H.P. Phatnani, P. Guarnieri, C. Caneda, N. Ruderisch, et al., An RNA-sequencing transcriptome and splicing database of glia, neurons, and vascular cells of the cerebral cortex, J. Neurosci. 34 (2014) 11929–11947, https://doi.org/10.1523/JNEUROSCI.1860-14.2014.
[61] W. Cai, D.A. Andres, mTORC2 is required for rit-mediated oxidative stress resistance, PLoS One 9 (2014), e115602, https://doi.org/10.1371/journal.pone.0115602.
[62] A.I. Flores, S.P. Narayanan, E.N. Morse, H.E. Shick, X. Yin, G. Kidd, R.L. Avila, D.A. Kirschner, W.B. Macklin, Constitutively active Akt induces enhanced myelination in the CNS, J. Neurosci. 28 (2008) 7174–7183, https://doi.org/10.1523/JNEUROSCI.0150-08.2008.
[63] S. Goebbels, J.H. Oltrogge, R. Kemper, I. Heilmann, I. Bormuth, S. Wolfer, S.P. Wichert, W. Mobius, X. Liu, C. Lappe-Siefke, et al., Elevated phosphatidylinositol 3,4,5-trisphosphate in glia triggers cell-autonomous membrane wrapping and myelination, J. Neurosci. 30 (2010) 8953–8964, https://doi.org/10.1523/JNEUROSCI.0219-10.2010.
[64] E.P. Harrington, C. Zhao, S.P. Fancy, S. Kaing, R.J. Franklin, D.H. Rowitch, Oligodendrocyte PTEN is required for myelin and axonal integrity, not remyelination, Ann. Neurol. 68 (2010) 703–716, https://doi.org/10.1002/ana.22090.
[65] W.A. Tyler, N. Gangoli, P. Gokina, H.A. Kim, M. Covey, S.W. Levison, T.L. Wood, Activation of the mammalian target of rapamycin (mTOR) is essential for oligodendrocyte differentiation, J. Neurosci. 29 (2009) 6367–6378, https://doi.org/10.1523/JNEUROSCI.0234-09.2009.
[66] S.E. Wahl, L.E. McLane, K.K. Bercury, W.B. Macklin, T.L. Wood, Mammalian target of rapamycin promotes oligodendrocyte differentiation, initiation and extent of CNS myelination, J. Neurosci. 34 (2014) 4453–4465, https://doi.org/10.1523/JNEUROSCI.4311-13.2014.
[67] S.A. Hoffmann, D. Hos, M. Kuspert, R.A. Lang, R. Lovell-Badge, M. Wegner, S. Reiprich, Stem cell factor Sox2 and its close relative Sox3 have differentiation functions in oligodendrocytes, Development 141 (2014) 39–50, https://doi.org/10.1242/dev.098418.
[68] S. Zhang, X. Zhu, X. Gui, C. Croteau, L. Song, J. Xu, A. Wang, P. Bannerman, F. Guo, Sox2 is essential for oligodendroglial proliferation and differentiation during postnatal brain myelination and CNS remyelination, J. Neurosci. 38 (2018) 1802–1820, https://doi.org/10.1523/JNEUROSCI.1291-17.2018.
[69] C. Zhao, D. Ma, M. Zawadzka, S.P. Fancy, L. Elis-Williams, G. Bouvier, J.H. Stockley, G.M. de Castro, B. Wang, S. Jacobs, et al., Sox2 sustains recruitment of oligodendrocyte progenitor cells following CNS demyelination and primes them for differentiation during remyelination, J. Neurosci. 35 (2015) 11482–11499, https://doi.org/10.1523/JNEUROSCI.3655-14.2015.
[70] B. Jablonska, M. Gierdalski, L.J. Chew, T. Hawley, M. Catron, A. Lichauco, J. Cabrera-Luque, T. Yuen, D. Rowitch, V. Gallo, Sirt1 regulates glial progenitor proliferation and regeneration in white matter after neonatal brain injury, Nat. Commun. 7 (2016), 13866, https://doi.org/10.1038/ncomms13866.
[71] M. Loix, E. Wouters, S. Vanherle, J. Dehairs, J.L. McManaman, H. Kemps, J.V. Swinnen, M. Haidar, J.F.J. Bogie, J.J.A. Hendriks, Perilipin-2 limits remyelination by preventing lipid droplet degradation, Cell. Mol. Life Sci. 79 (2022) 515, https://doi.org/10.1007/s00018-022-04547-0.
[72] S. Michan, Y. Li, M.M. Chou, E. Parrella, H. Ge, J.M. Long, J.S. Allard, K. Lewis, M. Miller, W. Xu, et al., SIRT1 is essential for normal cognitive function and synaptic plasticity, J. Neurosci. 30 (2010) 9695–9707, https://doi.org/10.1523/JNEUROSCI.0027-10.2010.
[73] A. Kamermans, M. Rijnsburger, A. Chakraborty, S. van der Pol, H.E. de Vries, J. van Horssen, Reduced angiopoietin-like 4 expression in multiple sclerosis lesions facilitates lipid uptake by phagocytes via modulation of lipoprotein-lipase activity, Front. Immunol. 10 (2019) 950, https://doi.org/10.3389/fimmu.2019.00950.
[74] T.R. Hammond, A. Gadea, J. Dupree, C. Kerninon, B. Nait-Oumesmar, A. Aguirre, V. Gallo, Astrocyte-derived endothelin-1 inhibits remyelination through notch activation, Neuron 81 (2014) 1442, https://doi.org/10.1016/j.neuron.2014.03.007.
[75] S. Schneider, A. Gruart, S. Grade, Y. Zhang, S. Kroger, F. Kirchhoff, G. Eichele, J.M. Delgado Garcia, L. Dimou, Decrease in newly generated oligodendrocytes leads to motor dysfunctions and changed myelin structures that can be rescued by transplanted cells, Glia 64 (2016) 2201–2218, https://doi.org/10.1002/glia.23055.
[76] R. Fledrich, T. Abdelaal, L. Rasch, V. Bansal, V. Schutza, B. Brugger, C. Luchtenborg, T. Prukop, J. Stenzel, R.U. Rahman, et al., Targeting myelin lipid metabolism as a potential therapeutic strategy in a model of CMT1A neuropathy, Nat. Commun. 9 (2018) 3025, https://doi.org/10.1038/s41467-018-05420-0.

[77] X. Zhou, C. He, J. Ren, C. Dai, S.R. Stevens, Q. Wang, D. Zamler, T. Shingu, L. Yuan, C.R. Chandregowda, et al., Mature myelin maintenance requires Qki to coactivate PPARbeta-RXRalpha-mediated lipid metabolism, J. Clin. Invest. 130 (2020) 2220–2236, https://doi.org/10.1172/JCI131800.
[78] H. Tanaka, J. Ma, K.F. Tanaka, K. Takao, M. Komada, K. Tanda, A. Suzuki, T. Ishibashi, H. Baba, T. Isa, et al., Mice with altered myelin proteolipid protein gene expression display cognitive deficits accompanied by abnormal neuron-glia interactions and decreased conduction velocities, J. Neurosci. 29 (2009) 8363–8371, https://doi.org/10.1523/JNEUROSCI.3216-08.2009.
[79] S.G. Waxman, Determinants of conduction velocity in myelinated nerve fibers, Muscle Nerve 3 (1980) 141–150, https://doi.org/10.1002/mus.880030207.
[80] X. Lee, Y. Hu, Y. Zhang, Z. Yang, Z. Shao, M. Qiu, B. Pepinsky, R.H. Miller, S. Mi, Oligodendrocyte differentiation and myelination defects in OMgp null mice, Mol. Cell. Neurosci. 46 (2011) 752–761, https://doi.org/10.1016/j.mcn.2011.02.008.
[81] A. Robaglia-Schlupp, J. Pizant, J.C. Norreel, E. Passage, D. Saberan-Djoneidi, J.L. Ansaldi, L. Vinay, D. Figarella-Branger, N. Levy, F. Clarac, et al., PMP22 overexpression causes dysmyelination in mice, Brain 125 (2002) 2213–2221, https://doi.org/10.1093/brain/awf230.
[82] A. Hayashi, N. Kaneko, C. Tomihira, H. Baba, Sulfatide decrease in myelin influences formation of the paranodal axo-glial junction and conduction velocity in the sciatic nerve, Glia 61 (2013) 466–474, https://doi.org/10.1002/glia.22447.
[83] H. Ramakrishnan, K.K. Hedayati, R. Lullmann-Rauch, C. Wessig, S.N. Fewou, H. Maier, H.H. Goebel, V. Gieselmann, M. Eckhardt, Increasing sulfatide synthesis in myelin-forming cells of arylsulfatase A-deficient mice causes demyelination and neurological symptoms reminiscent of human metachromatic leukodystrophy, J. Neurosci. 27 (2007) 9482–9490, https://doi.org/10.1523/JNEUROSCI.2287-07.2007.
[84] C. Lappe-Siefke, S. Goebbels, M. Gravel, E. Nicksch, J. Lee, P.E. Braun, I.R. Griffiths, K.A. Nave, Disruption of Cnp1 uncouples oligodendroglial functions in axonal support and myelination, Nat. Genet. 33 (2003) 366–374, https://doi.org/10.1038/ng1095.
[85] D.A. Andres, L.E.A. Young, S. Veeranki, T.R. Hawkinson, B.M. Levitan, D. He, C. Wang, J. Satin, R.C. Sun, Improved workflow for mass spectrometry-based metabolomics analysis of the heart, J. Biol. Chem. 295 (2020) 2676–2686, https://doi.org/10.1074/jbc.RA119.011081.
[86] M.K. Brewer, A. Uittenbogaard, G.L. Austin, D.M. Segvich, A. DePaoli-Roach, P.J. Roach, J.J. McCarthy, Z.R. Simmons, J.A. Brandon, Z. Zhou, et al., Targeting pathogenic lafora bodies in lafora disease using an antibody-enzyme fusion, Cell Metab (2019), https://doi.org/10.1016/j.cmet.2019.07.002.
[87] J.L. Sampaio, M.J. Gerl, C. Klose, C.S. Ejsing, H. Beug, K. Simons, A. Shevchenko, Membrane lipidome of an epithelial cell line, Proc Natl Acad Sci U S A 108 (2011) 1903–1907, https://doi.org/10.1073/pnas.1019267108.
[88] C.S. Ejsing, J.L. Sampaio, V. Surendranath, E. Duchoslav, K. Ekroos, R.W. Klemm, K. Simons, A. Shevchenko, Global analysis of the yeast lipidome by quantitative shotgun mass spectrometry, Proc Natl Acad Sci U S A 106 (2009) 2136–2141, https://doi.org/10.1073/pnas.0811700106.
[89] R. Herzog, K. Schuhmann, D. Schwudke, J.L. Sampaio, S.R. Bornstein, M. Schroeder, A. Shevchenko, LipidXplorer: a software for consensual cross-platform lipidomics, PLoS One 7 (2012), e29851, https://doi.org/10.1371/journal.pone.0029851.
[90] R. Herzog, D. Schwudke, K. Schuhmann, J.L. Sampaio, S.R. Bornstein, M. Schroeder, A. Shevchenko, A novel informatics concept for high-throughput shotgun lipidomics based on the molecular fragmentation query language, Genome Biol. 12 (2011) R8, https://doi.org/10.1186/gb-2011-12-1-r8.
[91] A.E. Stanback, L.R. Conroy, L.E.A. Young, T.R. Hawkinson, K.H. Markussen, H.A. Clarke, D.B. Allison, R.C. Sun, Regional N-glycan and lipid analysis from tissues using MALDI-mass spectrometry imaging, STAR Protoc 2 (2021), 100304, https://doi.org/10.1016/j.xpro.2021.100304.
[92] K.A. Berry, J.A. Hankin, R.M. Barkley, J.M. Spraggins, R.M. Caprioli, R.C. Murphy, MALDI imaging of lipid biochemistry in tissues by mass spectrometry, Chem Rev 111 (2011) 6491–6512, https://doi.org/10.1021/cr200280p.
[93] R.C. Murphy, J.A. Hankin, R.M. Barkley, Imaging of lipid species by MALDI mass spectrometry, J. Lipid Res. 50 (Suppl) (2009) S317–S322, https://doi.org/10.1194/jlr.R800051-JLR200.
[94] V. Carola, F. D'Olimpio, E. Brunamonti, F. Mangia, P. Renzi, Evaluation of the elevated plus-maze and open-field tests for the assessment of anxiety-related behaviour in inbred mice, Behav. Brain Res. 134 (2002) 49–57, https://doi.org/10.1016/s0166-4328(01)00452-1.
[95] H. Shiotsuki, K. Yoshimi, Y. Shimo, M. Funayama, Y. Takamatsu, K. Ikeda, R. Takahashi, S. Kitazawa, N. Hattori, A rotarod test for evaluation of motor skill learning, J. Neurosci. Methods 189 (2010) 180–185, https://doi.org/10.1016/j.jneumeth.2010.03.026.
[96] S.F. Martinez-Huenchullan, S.V. McLennan, L.A. Ban, M. Morsch, S.M. Twigg, C.S. Tam, Utility and reliability of non-invasive muscle function tests in high-fat-fed mice, Exp. Physiol. 102 (2017) 773–778, https://doi.org/10.1113/EP086328.